https://doi.org/10.5194/egusphere-2026-6720
Preprint. Discussion started: 5 November 2026
© Author(s) 2026. CC BY 4.0 License.

A–WALI: An Airborne Raman Lidar for Aerosol, Cloud, Temperature, and Water Vapor Observations during MAESTRO

Patrick Chazette, Julien Totems

LSCE/IPSL, CNRS-CEA-UVSQ, University Paris-Saclay, CEA Saclay, 91191 Gif sur Yvette, France

Correspondence to: patrick.chazette@lsce.ipsl.fr

Abstract. In preparation for the MAESTRO (Mesoscale Organisation of Tropical Convection) airborne campaign conducted off Cabo Verde in August–September 2024, the Airborne Weather and Aerosol Lidar (A-WALI) was developed to characterize the horizontal distributions of clouds, aerosols, water vapor, and atmospheric temperature through a side window of the SAFIRE ATR-42 research aircraft. This compact Raman lidar operates at 355 nm and combines a 15 cm telescope with a diode-pumped laser delivering 60 mJ pulses at a repetition rate of 200 Hz. Its measurement performance was assessed through end-to-end simulations, ground-based observations, and airborne measurements. A-WALI successfully resolves cloud and aerosol structures. Under nighttime conditions, water vapor mixing ratios can be retrieved over distances of approximately 2–3 km with a statistical uncertainty below 0.5 g kg^{-1}, while temperature retrievals achieve an uncertainty below 0.5 °C over distances of approximately 1 km. At shorter measurement ranges (≤ 2 km), fluctuations in water vapor and temperature can be resolved under both daytime and nighttime conditions. Comparisons with in situ measurements support the calibration and validation of the retrievals, demonstrating the potential of A-WALI to investigate the horizontal variability of atmospheric thermodynamic properties, clouds, and aerosols from an airborne platform.

Keywords: aerosols, clouds, water vapor, temperature, lidar, Raman, airborne

1 Introduction

To address key scientific questions related to the Earth's climate system at local to regional scales, the Airborne-Weather and Aerosol Lidar (A–WALI), was developed for deployment on the French research aircraft ATR–42 (https://www.safire.fr/, last access 30 October 2026). The targeted atmospheric variables include aerosols, clouds, water vapor, and temperature. While

https://doi.org/10.5194/egusphere-2026-6720
Preprint. Discussion started: 5 November 2026
© Author(s) 2026. CC BY 4.0 License.

airborne lidar measurements are not new, only a few Raman lidar systems have been deployed on aircrafts.

For aerosols and clouds samplings, Rayleigh-Mie lidars have been primarily used, such as LEANDRE–1 (Lidar pour l'Etude des Aerosols, des Nuages, de l'interaction Dynamique-Rayonnement et du cycle de l'Eau) (Pelon et al., 1988). This instrument was deployed in various campaigns, including the Surface of the ocean, fluxes and interaction with the atmosphere in the framework of the Atlantic stratocumulus transition experiment (SOFIA/ASTEX) (Chazette et al., 2001), the Indian Ocean Experiment (INDOEX) (Pelon et al., 2002) or Etude et Simulation de la qualité de l'air (ESQUIF) (Chazette et al., 2005). The Cloud Physics Lidar (CPL) has been built for use on the NASA ER-2 high-altitude aircraft to provide multiwavelength measurements of cirrus, subvisual cirrus, and aerosols (McGill et al., 2002). Another example is the ALEX lidar developed by DLR (Renger et al., 1997), which was deployed during several airborne research campaigns, including the Cloud Lidar and Radar Experiment (CLARE'98; Hogan et al., 2003) and the EU-funded programme Scientific Training and Access to Aircraft for Atmospheric Research Throughout Europe (STAAARTE; Dulac and Chazette, 2003). More recently, compact lidars such as ALiAS (Airborne Lidar for Aerosol Study) (Chazette et al., 2021) have been used in major international campaigns like Elucidating the role of cloud–circulation coupling in climate (EUREC4A) (Bony et al., 2022).

High spectral resolution lidars (HSRL) have recently been integrated into aircraft to better constrain the optical properties of clouds and aerosols. Notably, the Megacity Initiative: Local and Global Research Observations (MILAGRO) campaign included the NASA Langley Research Center (LaRC) airborne High Spectral Resolution Lidar (HSRL) (Rogers et al., 2009). This instrument also contributed to building the reference database for the Cloud-Aerosol Lidar with Orthogonal Polarization (CALIOP) (Burton et al., 2012). The LEANDRE New Generation (LNG) lidar (Bruneau et al., 2015) was recently used for the Aerosols, Radiation and Clouds in southern Africa (AEROCLO-sA) (Flamant et al., 2022) and for EUREC4A.

Atmospheric water vapor has also frequently been sampled using airborne lidar, but mostly with differential absorption lidar (DIAL) technology. The LEANDRE-2 lidar (Bruneau et al., 2001) was one of the key components of the Hydrological cycle in the Mediterranean eXperiment (HyMeX) (Lee et al., 2017). Another example is the German system airborne multi-wavelength water vapor differential absorption lidar (WALES) (Wirth et al., 2009) which flew during the Convective and Orographically-induced Precipitation Study (COPS) (Kiemle et al., 2011) and more recently during EUREC4A (Konow et al., 2021).

https://doi.org/10.5194/egusphere-2026-6720
Preprint. Discussion started: 5 November 2026
© Author(s) 2026. CC BY 4.0 License.

Airborne temperature measurements using rotational Raman lidar remain relatively rare. NASA developed a nadir-viewing airborne Raman lidar for the DC-8 and C-130 aircraft (Heaps and Burris, 1996), capable of simultaneously measuring water vapor and temperature. More recently, the University of Wyoming developed a compact rotational Raman temperature lidar operating also in a nadir-viewing configuration aboard a King Air aircraft for the Plains Elevated Convection At Night (PECAN) field campaign (Wu et al., 2016). Using a 355 nm laser emitting 50 mJ pulses at a repetition rate of 30 Hz, the Compact Rotational Lidar (CRL) provided nighttime nadir temperature profiles in the lower troposphere around developing convective systems. At night, a random temperature uncertainty below 0.5 K was achieved up to 800 m below the aircraft using a 45 m range resolution and a 1 km along-track integration. Finally, it is worth mentioning the parallel development of the Multi-function Airborne Raman Lidar (MARLi) by the same research group responsible for the PECAN instrument. MARLi is designed for nadir-looking measurements within the framework of the NASA Airborne Science Program (https://airbornescience.nasa.gov/instrument/Multi-function_Airborne_Raman_Lidar, last access: 5 August 2026).

This article presents and assesses the performance of the A–WALI Raman lidar, which was designed for horizontal measurements from the ATR–42 aircraft to characterize temperature, humidity, aerosol, and cloud fields during the Mesoscale Organisation of Tropical Convection (MAESTRO) campaign conducted off Cabo Verde in summer 2024. Horizontal aerosol and cloud structures had previously been investigated from the same aircraft during EUREC4A using the ALiAS lidar (Chazette et al., 2020). These observations highlighted the need for complementary measurements of water vapor and temperature to better characterize the thermodynamic environment associated with the mesoscale organization of convective cloud fields (Bony et al., 2022). Section 2 describes the lidar design, while Section 3 presents its expected performance based on end-to-end simulations. Section 4 evaluates the actual measurement uncertainties using ground-based and airborne observations and comparisons with in situ measurements. Conclusions are given in Section 5.

2 The A–WALI airborne Raman lidar

2.1 A–WALI design requirement

For measurements aboard the SAFIRE ATR–42 aircraft (https://www.safire.fr, last access: 19 September 2026), the scientific requirements of the MAESTRO campaign required a lidar system delivering an average power of at least 10 W at 355 nm and equipped with five detection channels: one elastic channel, two rotational Raman (RR) channels, and two vibrational Raman

https://doi.org/10.5194/egusphere-2026-6720
Preprint. Discussion started: 5 November 2026
© Author(s) 2026. CC BY 4.0 License.

(VR) channels (N_2 and H_2O). This configuration was designed to characterize clouds and aerosols and to measure water vapor and temperature fluctuations, up to 2 km transverse to the flight path. However, the practical constraints associated with airborne operation had the strongest influence on the lidar design. The lidar had to withstand accelerations of up to 9 g along the aircraft main axis and 7 g laterally. The total optical aperture had to be limited to 150 × 210 mm^2 to accommodate the dimensions of the side window; the overall system had to fit within a standard 19-inch rack; the payload was limited to 120 kg; and the average power consumption was limited to 1.2 kW. The lidar also had to be robust against dust, vibrations, and temperature fluctuations.

The main characteristics of the A-WALI system are summarized in Table 1, and its overall design is shown in Figure 1.

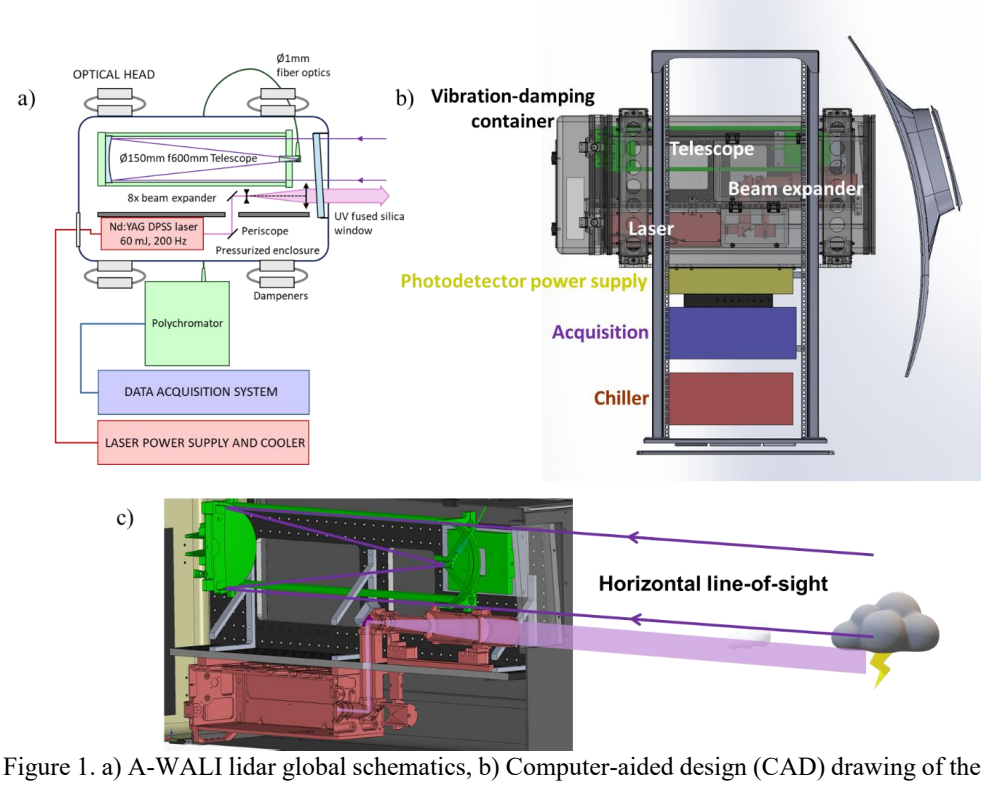


Figure 1. a) A-WALI lidar global schematics, b) Computer-aided design (CAD) drawing of the full system in a standard rack behind the ATR-42 airplane window, c) Cutaway CAD drawing of the optical head.

Table 1: Main characteristics of the A-WALI airborne lidar.

	A–WALI
Emitted wavelength (nm)	354.67

https://doi.org/10.5194/egusphere-2026-6720
Preprint. Discussion started: 5 November 2026
© Author(s) 2026. CC BY 4.0 License.

Elastic channels (parallel – perpendicular)	
Central wavelength of filter (CWL) (nm)	354.77 – 354.78
Filter bandwidth (FWHM) (nm)	0.24 – 0.23
Transmission	60% – 60%
Rovibrational Raman channels (N_2 – H_2O)	
Central wavelength of filter (CWL) (nm)	386.80 – 407.63
Filter bandwidth (FWHM) (nm)	0.21 – 0.35
Transmission	86% – 70%
Rotational Raman channels (RR1 – RR2)	
Central wavelength of filter (CWL) (nm)	354.10 – 353.24
Filter bandwidth (FWHM) (nm)	0.21 – 0.45
Transmission	55% – 60.6%
General characteristics	
Emitted energy (mJ)	60
Repetition rate (Hz)	200
Telescope diameter (mm)	150
Telescope field-of-view (mrad)	2.1
Laser divergence (mrad)	0.2
Native range resolution (m)	0.75
Final range resolution (m)	12 – 100
Minimum range (m)	200
Native time resolution (s)	2 – 4
Final time resolution (s)	2 – 15

2.2 A–WALI emission system

Pulses from a Lumibird Merion C-G5 laser, delivering 60 mJ at 355 nm at a repetition rate of 200 Hz, are directed through a periscope incorporating two additional harmonic-separator dichroic mirrors (EKSMA 042-3515), with a reflectivity greater than 99.5% at 355 nm and lower than 5% at 532 and 1064 nm. This configuration strongly suppresses the residual visible and near-infrared radiation and ensures eye-safe operation immediately outside the aircraft.

The laser is not injection-seeded, as this would not have been feasible given the instrumental constraints described above. Consequently, a drift in the absolute temperature retrieved from the lidar measurements may occur, together with greater leakage of elastic backscatter into the RR channels (Behrendt, 2006). However, the main scientific objective is to resolve relative temperature fluctuations, whereas the absolute temperature near the aircraft is independently constrained by accurate in situ measurements. In addition, elastic leakage into the RR channels can be quantified and corrected.

An 8× beam expander, composed of two off-the-shelf UV fused-silica lenses (Edmund Optics #48052 and Thorlabs LC4855-UV), is used to increase the beam diameter to 40 mm. The lenses are mounted in low-profile slip-plate positioners to minimize the separation between the

https://doi.org/10.5194/egusphere-2026-6720
Preprint. Discussion started: 5 November 2026
© Author(s) 2026. CC BY 4.0 License.

emission beam expander and the receiver telescope, as constrained by the dimensions of the aircraft window, while still allowing optical alignment. The beam divergence is optimized by imaging the beam with a camera positioned at the focal plane of the receiver telescope, resulting in a full beam divergence of less than 0.2 mrad RMS.

The residual energy in the visible and near-infrared spectral ranges is extremely low owing to the dichroic periscope, although weak green flashes remain visible. The system is therefore classified as Class 2M according to NF EN IEC 60825-1:2014.

2.3 A–WALI receiver and polychromator

A UV-enhanced aluminium-coated Ø152.4 mm F/4 parabolic reflector (substrate from Edmund Optics, coating by Kerdry) is used to focus the collected light into a 1-mm-diameter multimode optical fiber (Avantes, high-OH, solarization-resistant), resulting in a receiver field of view of 1.64 mrad in diameter. The optical fibre is coupled laterally into the receiver shortly after a 90° reflection from a small prism mirror with high reflectivity in the near-UV.

The optical fiber feeds the compact polychromator shown schematically in Figure 2. Although this design is not optimal in terms of transmission through the RR channels, it enables a very compact optical setup. The collimated beam diameter of approximately 13 mm allows the use of standard 1-inch and 25 × 36 mm^2 filters and beamsplitters within a standard cage system. Each filter–lens–PMT assembly is jointly mounted on a tip-tilt platform, allowing compensation for angular misalignments introduced by the beamsplitters. This adjustment is performed by autocollimation on the optical fibre output.

Upstream of each photomultiplier tube (PMT), an assembly of two UV fused-silica lenses reduces the beam diameter to approximately 6 mm while maintaining the PMT surface close to the pupil plane, thereby avoiding range-dependent biases as discussed in Totems et al. (2021). The elastic channel is obtained by reflection from the RR1 and RR2 interference filters, both of which exhibit high reflectivity at 354.7 nm to prevent elastic backscatter contamination in the RR channels. Potential interference effects associated with the quasi-Michelson geometry of the left optical arm were investigated but found to be negligible by imaging the elastic-channel output under laser illumination. This is likely because the optical path difference exceeds the coherence length of the laser.

https://doi.org/10.5194/egusphere-2026-6720
Preprint. Discussion started: 5 November 2026
© Author(s) 2026. CC BY 4.0 License.

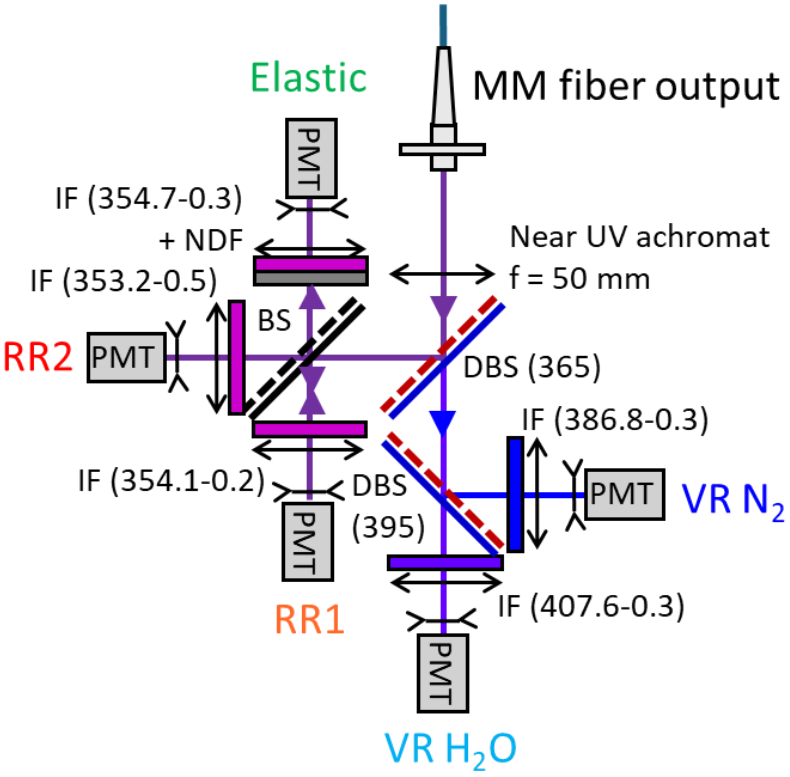


Figure 2. Polychromator setup. The Elastic channel is obtained by the reflection on the RR1 and RR2 filters. BS: 50/50 beam-splitter, DBS: dichroic beam–splitter (with cut-on wavelength in nm in parentheses), IF: interference filter (with central wavelength and full width at half maximum in nm in parentheses), NDF: neutral density filter (anti-reflection coated, absorptive), PMT: photo-multiplier tube (detector). VR: vibrational Raman, RR: rotational Raman channels.

3 End-to-end modelling

To evaluate the statistical biases and uncertainties associated with the A–WALI lidar, a digital twin of the instrument was developed, accounting for the instrument characteristics, typical atmospheric conditions, and Raman scattering. Also referred to as an end-to-end simulator, it integrates both the forward simulation of the lidar signals and the inversion methods required to retrieve the geophysical parameters. It is an essential tool not only for instrument design but also for quantifying the different sources of uncertainty.

3.1 Direct signal

3.1.1 General equation

Depending on the horizontal distance from the aircraft, x, and the altitude, z, the lidar signal S_i measured in channel i can be expressed in the general form for a line of sight inclined at an angle θ to the horizontal:

https://doi.org/10.5194/egusphere-2026-6720
Preprint. Discussion started: 5 November 2026
© Author(s) 2026. CC BY 4.0 License.

$$S_i(x,z) = \frac{C_i}{x^2} \cdot O_i(x) \cdot \left(\beta_{m,i}(x,z) + \varepsilon_i \cdot [\beta_a(x,z) + \beta_c(x,z)]\right) \cdot \exp\left[-\frac{2}{\cos(\theta(z))} \cdot \left(\tau_{m,i}(\mathrm{x},\mathrm{z}) + \tau_{a,i}(\mathrm{x},\mathrm{z}) + \tau_{c,i}(\mathrm{x},\mathrm{z})\right)\right] + BR_i(z) \quad (1)$$

with the optical thickness $\tau_{k,i}$ defined as a function of the extinction coefficient $\alpha_{k,i}$ by the relationship:

$$\tau_{k,i}(\mathrm{x},z) = \int_0^{\mathrm{x}} \alpha_{k,i}(x',\mathrm{z}) \cdot dx' \quad (2)$$

Each lidar channel is associated with a system constant C_i and an overlap function O_i. BR_i is the background radiation signal. The laser beam propagates through the atmosphere, where it is backscattered by air molecules (subscript *m*), aerosols (subscript *a*), and/or clouds (subscript *c*) towards the receiving system. The interaction with the atmospheric medium is characterized by the volume backscattering coefficient $\beta_{k,i}$ (k = *m*, *a*, or *c*). For the elastic channel ($i = E$), contributions from aerosols and clouds are considered ($\varepsilon_i = 1$), whereas for the Raman channels, only the molecular contribution is considered ($\varepsilon_i = 0$). For the elastic channel, the backscatter coefficient $\beta_{m,i}$ corresponds to the molecular backscatter coefficient, as defined by Nicolet (1984). For the Raman channels, it corresponds to the Raman backscatter coefficient, which is proportional to the Raman backscatter cross section and the molecular concentration.

For water vapor and temperature measurements, two Raman channel pairs are used. The vibro-rotational channels for nitrogen ($i = N_2$) and water vapor ($i = H_2O$) are used to determine the water vapor mixing ratio (WVMR), while two rotational channels ($i = RR1$ and $i = RR2$) are used to retrieve the thermodynamic air temperature. For temperature measurements, two spectral regions with different temperature sensitivities are selected in the anti-Stokes rotational Raman lines, to avoid leaking of the elastic line on rays impacting the filters with an angle.

3.1.2 Calibration of Forward-Simulated Lidar Signals

To calibrate the digital twin, i.e. to account for realistic system constants C_i, horizontal measurements were performed from the laboratory. Temperature, water vapor mixing ratio (WVMR), and aerosol extinction were measured simultaneously outside the building. These atmospheric parameters may vary along the line of sight. To minimize such variations, the measurements were performed at night, with the lidar pointing above bare ground (open fields) to mitigate the effects of turbulence. Moreover, the 15-min period exhibiting the lowest variability in the lidar signals was selected to determine the system constants.

The results are presented in Figure 3 for an integration time of 2 s over the first 5 km. Very good agreement is observed between the numerical simulation and the measurements. For the

https://doi.org/10.5194/egusphere-2026-6720
Preprint. Discussion started: 5 November 2026
© Author(s) 2026. CC BY 4.0 License.

H_2O–Raman channel, however, the measurement range remains limited to approximately 2 km under conditions characterized by a WVMR of 3.9 g kg^{-1} and an aerosol extinction coefficient (AEC) of ~0.09 km^{-1}.

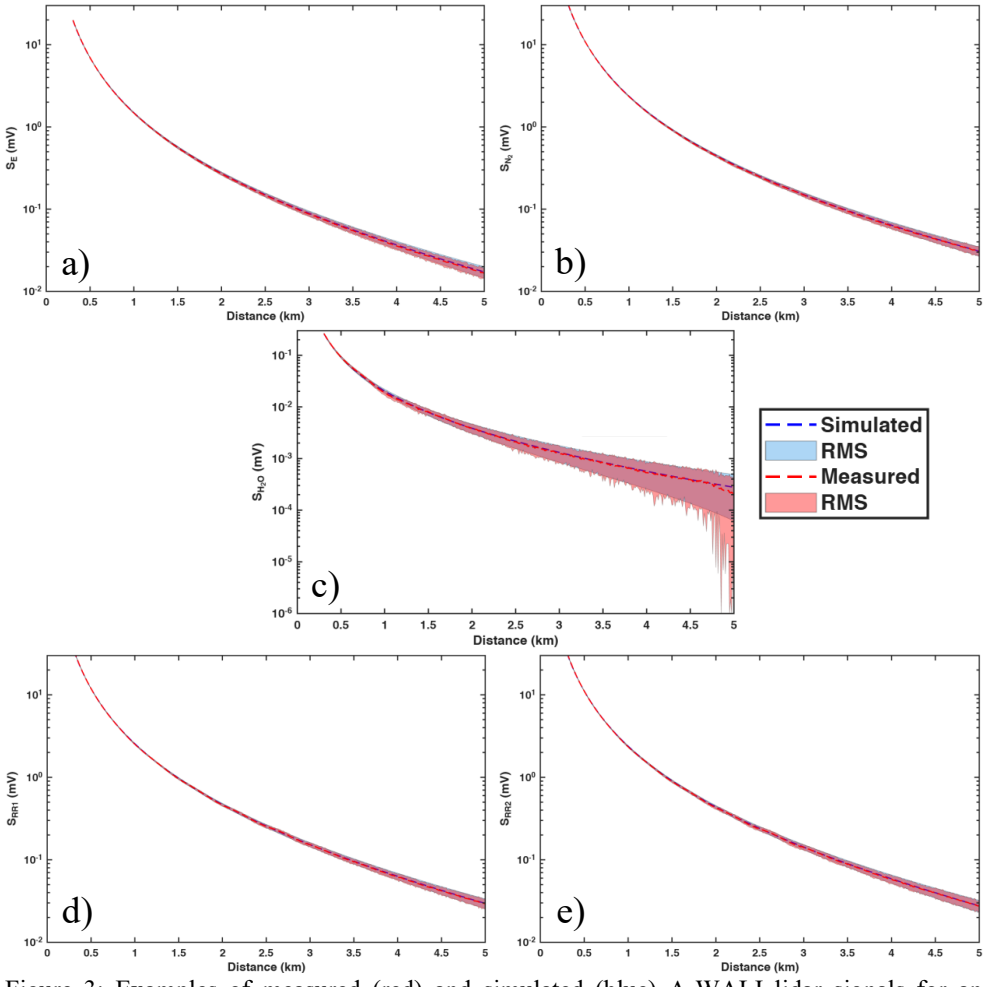


Figure 3: Examples of measured (red) and simulated (blue) A-WALI lidar signals for an integration time of 2 s: a) elastic, b) N_2–Raman, c) H_2O–Raman, d) RR1, and e) RR2 channels. The load resistance is 50 Ω in this case.

3.2 Inverse signal

The geophysical parameters are retrieved from the system of equations given in Eq. (1). This section describes the retrieval methods, while the results are presented later.

https://doi.org/10.5194/egusphere-2026-6720
Preprint. Discussion started: 5 November 2026
© Author(s) 2026. CC BY 4.0 License.

3.2.1 Aerosols

Based on horizontal lidar measurements, the procedure described by Chazette et al. (2020) for retrieving the AEC close to the aircraft, $\alpha_a(z)$, is directly applied to the elastic and rotational Raman channels using the following relationship:

$$\alpha_a(z) = -\frac{1}{2}\frac{\partial log\left(R_{app}(x,z)\right)}{\partial x} \quad (3)$$

where the apparent scattering ratio (ASR) R_{app} is given by

$$R_{app}(x,z) = \frac{x^2}{\beta_{m,i}(x,z)} \cdot (S_i(x,z) - BR_i(z)) \cdot \exp\left[\frac{2}{\cos(\theta(z))} \cdot \left(\tau_{m,i}(\mathrm{x},\mathrm{z})\right)\right] \quad (4)$$

This approach assumes that the optical properties remain constant over the first kilometer from the aircraft. The derivative is estimated using a linear least-squares fit, and fits with an uncertainty greater than 0.01 km^{-1} are discarded. Sighting angles exceeding 5° are excluded. When applied to the N_2–Raman channel, the retrieval becomes increasingly biased as the aerosol Ångström exponent increases. However, the bias remains acceptable in the presence of desert aerosols.

3.2.2 Water vapor

For horizontal lidar measurements, the WVMR r_{H_2O} described by Chazette et al. (2025) is given by:

$$r_{H_2O}(x,z) = K \cdot R(x,z) \quad (5)$$

where

$$R(x,z) = O_R(x) \cdot \frac{S_{H_2O}(x,z)}{S_{N_2}(x,z)} \cdot \mathrm{C}_m(\mathrm{x},\mathrm{z}) \cdot \mathrm{C}_a(\mathrm{x},\mathrm{z}) \cdot \mathrm{C}_c(\mathrm{x},\mathrm{z}) \quad (6)$$

and the transmission correction factors C_k (k = m, a or c) are set by

$$C_k(x,z) = exp\left(\left[\eta_{k,H_2O}(\mathrm{z}) - \eta_{k,N_2}(z)\right] \cdot \int_0^x \alpha_k(\mathrm{x},\mathrm{z}) \cdot dx'\right) \quad (7)$$

with:

- K the calibration constant determined by comparison with airborne in situ measurements,
- $O_R(x) = \frac{O_{N_2}(x)}{O_{H_2O}(x)}$, the ratio of the overlap factors for the N_2– and H_2O– Raman channels,
- $\eta_{k,N_2}(z) = \left(\frac{386.8}{354.67}\right)^{-A_k(z)}$ and $\eta_{k,H_2O}(z) = \left(\frac{407.63}{354.67}\right)^{-A_k(z)}$, $A_k(z)$ is the Ångström exponent, with a value of 4.09 for molecular scattering, typically ranging between 0 and 2 for aerosols, and close to 0 for clouds, leading to $\mathrm{C}_c(\mathrm{x},z) \approx 1$.

https://doi.org/10.5194/egusphere-2026-6720
Preprint. Discussion started: 5 November 2026
© Author(s) 2026. CC BY 4.0 License.

3.2.3 Temperature

The atmospheric temperature, *T(x,z)*, is generally a nonlinear function of the ratio of the rotational Raman signals:

$$Q(x,z) = \frac{S_{RR2}(x,z)}{S_{RR1}(x,z)} \tag{8}$$

The differential Raman backscattering cross sections for the diatomic molecules N_2 and O_2 are calculated directly from molecular spectroscopy principles, following Penney et al. (1974). The values weighted by the atmospheric abundances of N_2 and O_2 are shown in Figure 4a for an air temperature of 20 °C. The transmission functions of the interference filters are also plotted. The differential Raman backscattering cross section of the RR1–Raman channel decreases with increasing temperature, whereas the opposite behavior is observed for the RR2–Raman channel (Figure 4b). This opposite temperature dependence ensures a high sensitivity of the *Q* ratio to temperature.

It is worth noting that the RR1 and RR2 channels can be combined to produce a signal with only weak temperature dependence. This combination is also shown for A–WALI in Figure 4b and can be used to correct for atmospheric transmission effects.

To minimize calibration-related biases, the temperature is expressed using the relationship proposed by Gerasimov and Zuev (2016) :

$$T(x,z) = \frac{c}{ln(Q(x,z))^2 + b\,ln(Q(x,z)) + a} \tag{9}$$

where

$$Q(x,z) = \exp\left[\frac{-b - \sqrt{b^2 - 4\left(a - \frac{c}{T(x,z)}\right)}}{2}\right] \tag{10}$$

The coefficients *a*, *b*, and *c* are derived from regression analyses between lidar measurements and reference measurements obtained from radiosondes or in-flight instruments (see section 4).

https://doi.org/10.5194/egusphere-2026-6720
Preprint. Discussion started: 5 November 2026
© Author(s) 2026. CC BY 4.0 License.

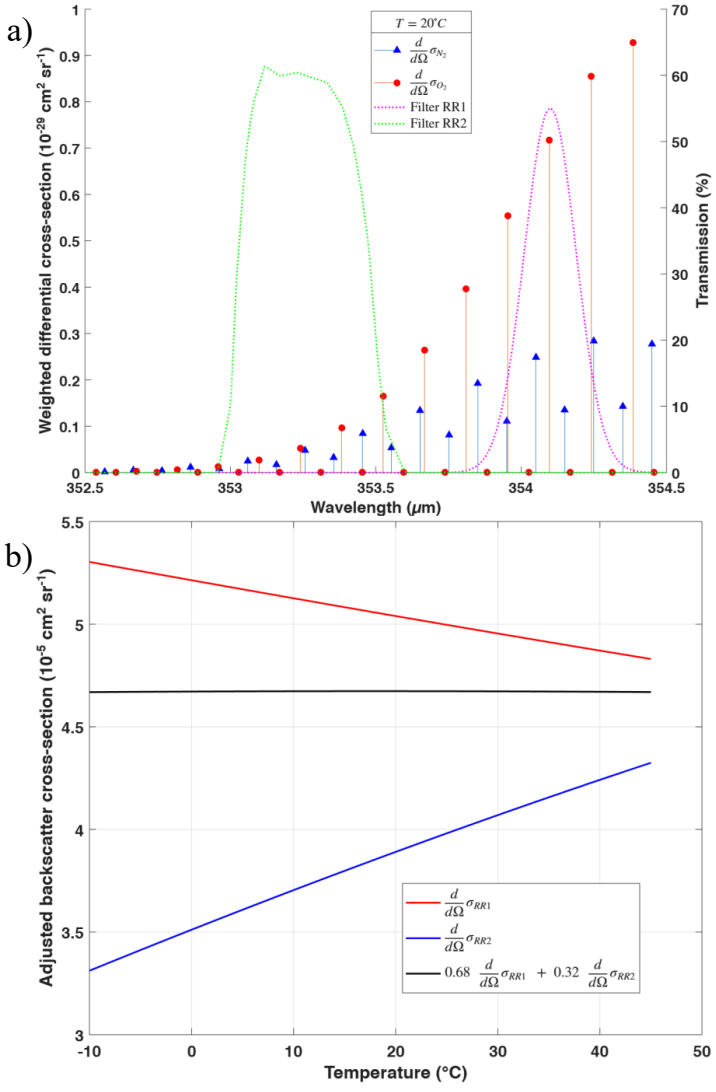


Figure 4. (a) Backscattering cross sections of rotational Raman lines of dioxygen ($\frac{d\sigma_{N_2}}{d\Omega}$, red) and dinitrogen ($\frac{d\sigma_{O_2}}{d\Omega}$, blue) at a temperature of 20 °C. The transmission functions of the rotational Raman interference filters are shown in purple (RR1) and green (RR2). (b) Temperature dependence of the Raman backscattering cross sections associated with the RR1 ($\frac{d\sigma_{RR1}}{d\Omega}, red$) and RR2 ($\frac{d\sigma_{RR2}}{d\Omega}, blue$) rotational Raman lidar channels. The combination of the RR1 and RR2 channels yielding a nearly temperature-independent response is shown in black.

3.3 Uncertainty sources

Potential sources of bias are discussed in this section, along with the approaches used to mitigate their effects. The procedure used to estimate the uncertainties is also presented.

https://doi.org/10.5194/egusphere-2026-6720
Preprint. Discussion started: 5 November 2026
© Author(s) 2026. CC BY 4.0 License.

3.3.1 Biases

Fiber fluorescence

Elastic scattering induces fluorescence in an OH-poor fiber at a non-negligible level compared with atmospheric Raman scattering (Sherlock et al., 1999; Whiteman et al., 2012). For this reason, an OH-rich fiber is used in A-WALI, resulting in a negligible source of bias compared with the other sources (Totems et al., 2021).

Electronic baseline

The baseline induced by the detection chain is found to vary between channels and over time. It is also subject to electromagnetic interference, causing parasitic signals at both high and low frequencies, due to laser emission and other neighbouring electronic devices. The grounds were interconnected and the detector lines were shielded and braided to minimize noise caused by external interference. The channel baselines are evaluated every 100 s, smoothed, and corrected. The resulting relative bias is therefore lower than 0.02% and can be neglected.

Background sky radiance and dark count

This signal offset is corrected using the pre-trigger recording, resulting in a negligible residual bias. In addition, the photomultiplier tubes were selected to minimize the dark count rate to less than 15 counts per second. In analog detection mode, the dark count rate is negligible. It should also be noted that the sky background radiance is lower for horizontal measurements than for zenith-pointing measurements.

Atmospheric temperature sensitivity of the H_2O Raman channel

Over a flight, atmospheric temperature variations can exceed 30 °C, resulting in variations in the Raman backscattering cross section of the H_2O channel. This introduces an altitude-dependent bias in the retrieved WVMR. The sensitivity of the N_2 channel to temperature is much lower and can be neglected (Whiteman, 2003). Figure 5a shows the roto-vibrational Raman lines of water vapor (Avila et al., 2004; Adam, 2009), together with the transmission function of the interference filter used, for an arbitrary temperature of 20 °C. The temperature dependence of the Raman backscattering cross section for the interference filter used is shown in Figure 5b. Over a temperature range of 40 °C, the variability reaches approximately 1.6% and must therefore be corrected. This correction is applied prior to the determination of the calibration constant K (Eq. 5). The resulting residual bias is very small, well below 0.1%.

https://doi.org/10.5194/egusphere-2026-6720
Preprint. Discussion started: 5 November 2026
© Author(s) 2026. CC BY 4.0 License.

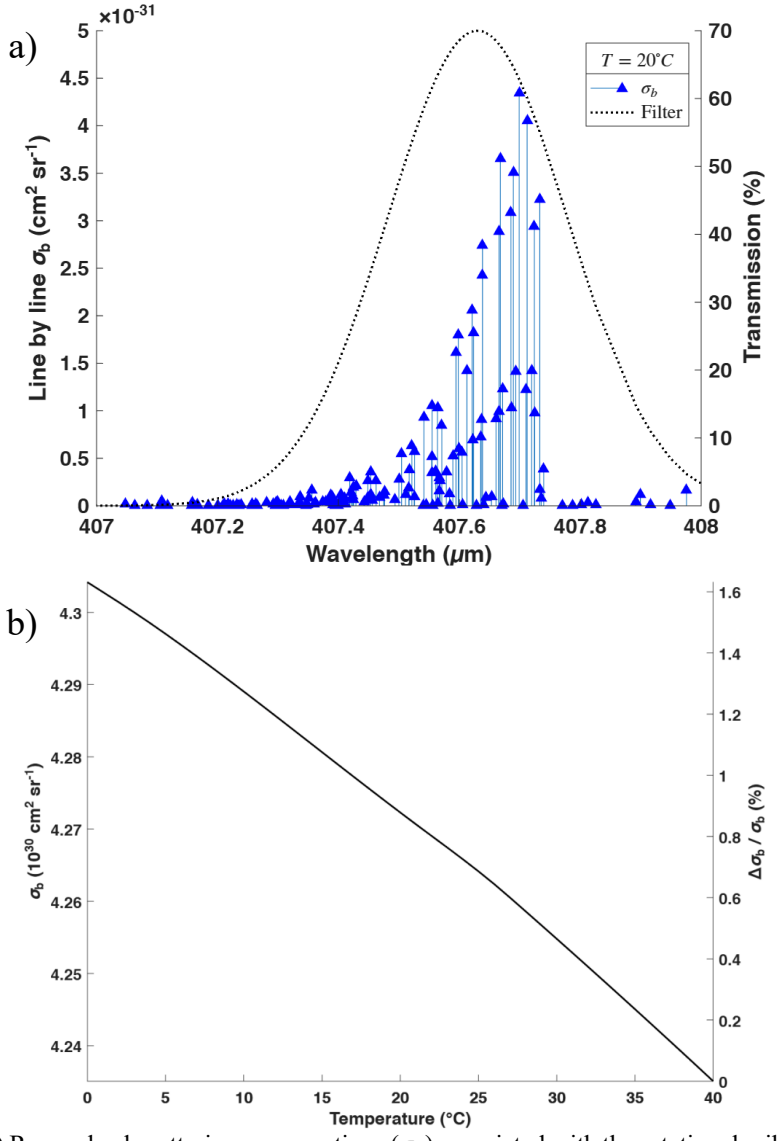


Figure 5. a) Raman backscattering cross sections (σ_b) associated with the rotational–vibrational Raman lines of water vapor (blue) at a temperature of 20 °C. The transmission function of the H_2O Raman interference filter is shown in black. (b) Temperature dependence of σ_b accounting for the filter transmission, and its relative variability ($\Delta\sigma_b/\sigma_b$): $\sigma_b = (-6.859\ 10^{-6} \cdot T^2 - 1.449\ 10^{-3} \cdot T + 4.304) \cdot 10^{-30}$ in $cm^2\ sr^{-1}$, with a Pearson correlation coefficient of 0.99.

Aerosol influence on the H_2O Raman channel

This aspect was investigated during WaLiNeAs for several zenith-pointing lidars deployed around the western Mediterranean (Chazette et al., 2026). For horizontal measurements, the effect of aerosols is corrected by integrating the extinction coefficient determined in Section 3.2.1 along the horizontal line of sight. Neglecting this correction leads to significant biases

https://doi.org/10.5194/egusphere-2026-6720
Preprint. Discussion started: 5 November 2026
© Author(s) 2026. CC BY 4.0 License.

that increase with both the aerosol extinction coefficient and the Ångström exponent (Figure 6). The correction was applied assuming that the extinction coefficient remains constant along the horizontal line of sight. The residual bias associated with this assumption is difficult to quantify accurately. However, assuming a variability comparable to that observed during constant-altitude flight legs, local variations of approximately 0.1 km^{-1} may occur, leading to biases of less than 1%. In this study, the N_2– and RR1–Raman channels can be used to better quantify the aerosol contribution.

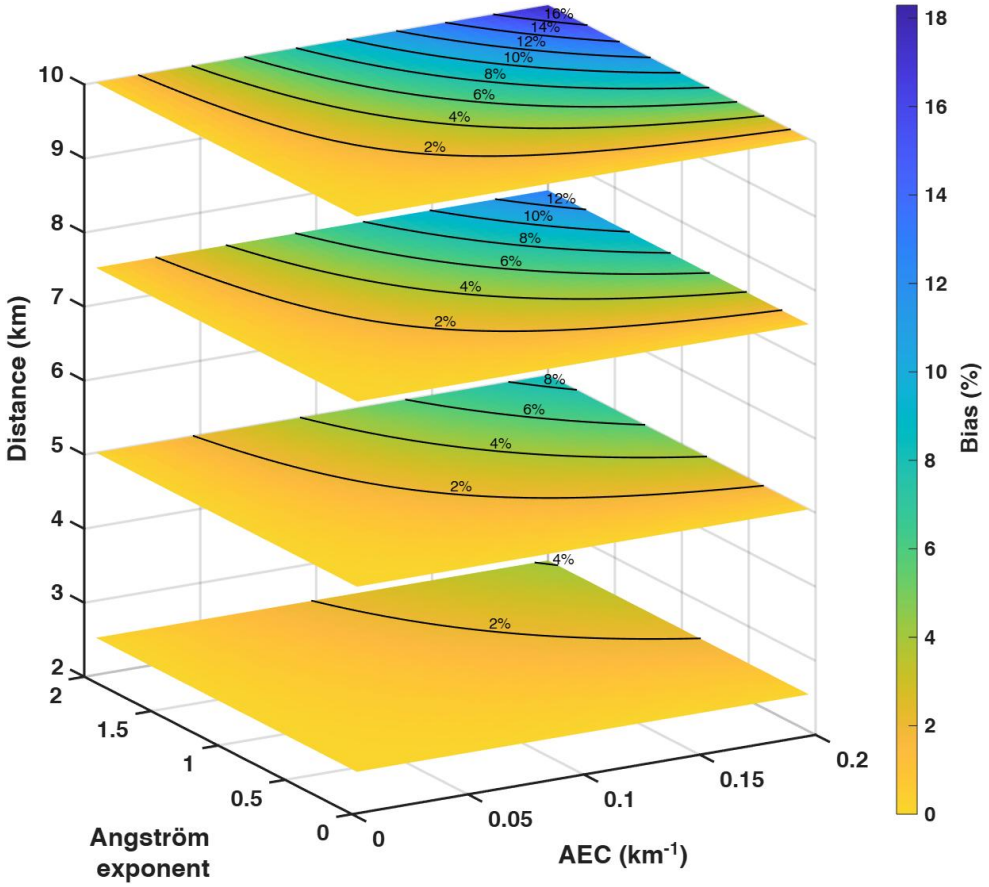


Figure 6. Relative bias in the water vapor mixing ratio due to the presence of aerosols at four distances from the aircraft. The bias depends on both the Ångström exponent and the aerosol extinction coefficient (AEC).

Laser and interference filter stability

Laser wavelength drift and interference filter central wavelength (CWL) drift due to temperature variations inside the aircraft mainly affect *Q*. For example, a 3 pm drift in either

https://doi.org/10.5194/egusphere-2026-6720
Preprint. Discussion started: 5 November 2026
© Author(s) 2026. CC BY 4.0 License.

the filter or laser wavelength can lead to biases exceeding 1°C (Totems et al., 2021). The wavelength drift of the interference filters used in A–WALI, manufactured by Materion, is approximately 1.3 pm $°C^{-1}$. During a given flight, the cabin temperature remains stable within 2 °C; however, it can vary significantly from one flight to another depending on meteorological conditions and the instruments in operation. This variability makes an independent calibration necessary for each flight.

Calibration

Calibration errors can represent one of the most significant sources of bias. Three calibrations are required for the A–WALI lidar: (i) the determination of the overlap factor between the emission and reception fields of view, which affects measurements at short distances from the aircraft; (ii) the water vapor calibration used to determine K (Eq. 5); and (iii) the temperature calibration used to determine the three coefficients a, b, and c (Eq. 9). The calibration results are presented in the following section.

3.3.2 Statistical uncertainties

The dominant source of statistical uncertainty in the A-WALI retrievals is the noise in the detected lidar signals. These uncertainties are estimated using a Monte Carlo approach, as in Royer et al. (2011). The calculations are based on nighttime measurements and therefore represent the lowest noise levels expected under conditions of negligible background light. The noise levels used in the Monte Carlo simulations are prescribed from the RMS signals fitted to the nighttime measurements shown in in Figure 3. Under daytime flight conditions, sky background radiance leads to a significant increase in statistical uncertainty. For a horizontally pointing airborne lidar, this background can vary considerably depending on the aircraft's orientation relative to the Sun, the time of day, cloud cover and its spatial variability, and flight altitude. The resulting degradation in the signal-to-noise ratio (SNR) inevitably reduces the lidar measurement range. Nighttime measurements will therefore be favored whenever possible, while the impact of sky background radiance on lidar observations will be clearly illustrated in Section 4.1.4.

The resulting uncertainties are discussed in more detail for each retrieved geophysical parameter. In the following, the RMS deviation from the mean is used to quantify statistical uncertainty.

Aerosol

Uncertainty simulations for the AEC are performed using a temporal integration of 2 s, corresponding to 400 laser shots. An AEC of 0.087 km^{-1}, encountered during the field

https://doi.org/10.5194/egusphere-2026-6720
Preprint. Discussion started: 5 November 2026
© Author(s) 2026. CC BY 4.0 License.

experiment, is considered as the true value. As shown in Figure 7, the RMS remains below 0.01 km^{-1}, as previously reported by Chazette et al. (2022). However, it is sufficiently large to result in a significant overlap between the AECs retrieved at 355 and 387 nm for an Ångström exponent of 0.5, as considered here for aerosols dominated by desert particles. Therefore, the use of these two wavelengths does not provide sufficient discrimination. Similar results are obtained for the elastic and rotational Raman (RR) channels. However, the RR channels are less sensitive to fluctuations associated with aerosol heterogeneity, resulting in RMS approximately 30% lower than those obtained for the elastic channel.

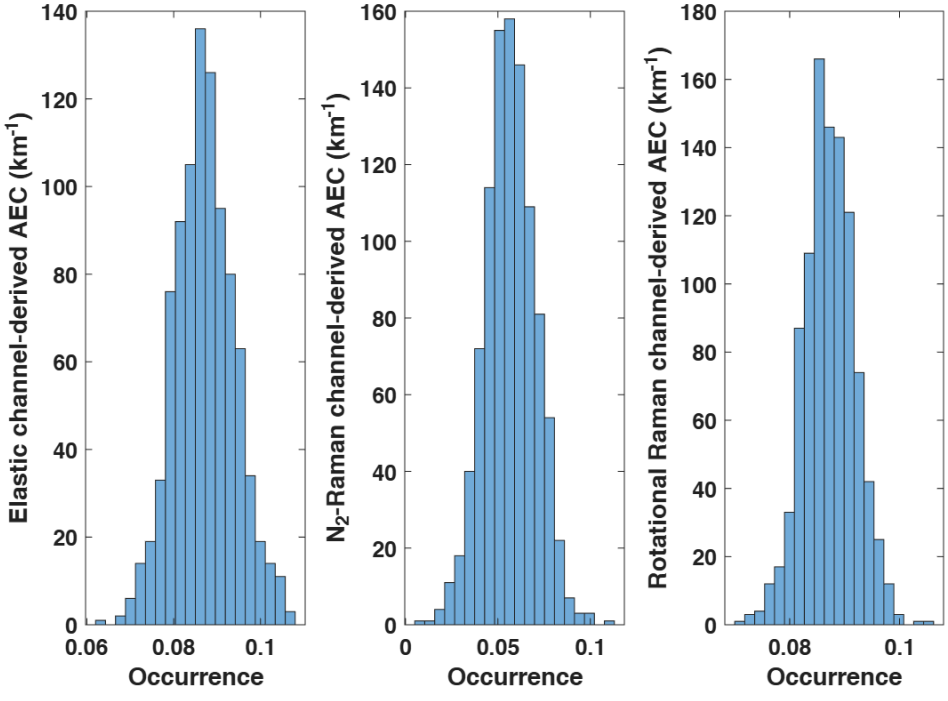


Figure 7. Occurrence of the aerosol extinction coefficient (AEC) retrieved from (a) the elastic, (b) the N_2–Raman, and (c) the rotational channels for 1000 noise realizations based on a 2-s integration time and an initial AEC value of 0.087 km^{-1}.

Water vapor and temperature

Two integration times were considered to evaluate the RMS on the WVMR with a range resolution of 100 m. The first, 2 s, corresponds to the temporal resolution targeted for sampling water vapor fields between clouds from an ATR-42 aircraft flying at a true airspeed of approximately 100 m s^{-1}, considering that the characteristic distance between shallow cumulus clouds ranges from 1 to 5 km (Koren et al., 2024). In practice, one profile is acquired every 200–300 m, as additional time is required for data formatting and storage, and especially for

https://doi.org/10.5194/egusphere-2026-6720
Preprint. Discussion started: 5 November 2026
© Author(s) 2026. CC BY 4.0 License.

the regular acquisition of the baseline, even though these processes are parallelized. The second integration time, 15 s, provides a more synoptic view of the water vapor and temperature fields, with sampling along the aircraft flight path approximately every 1.5 km. It is worth noting that an integration time of 15 s with a range resolution of 12 m provides approximately the same signal-to-noise ratio as an integration time of 2 s with a range resolution of ~100 m.

The RMS error values are shown in Figure 8a and 9b for WVMR and temperature, respectively. The AEC is set to 0.1 km^{-1} in all cases, close to the values observed in the lower troposphere during MAESTRO. A substantial difference is observed between the two temporal resolutions considered, resulting in significantly different measurement ranges.

In the presence of trade-wind cumulus clouds, organized updrafts typically exhibit a water vapor mixing ratio anomaly of approximately 0.5 g kg^{-1} and a temperature anomaly of approximately -0.1 °C relative to the horizontal mean, according to LeMone and Pennell (1976). More recently, following the EUREC4A field campaign (Bony et al., 2017), Brilouet et al. (2021) used airborne in situ measurements to highlight WVMR and temperature variations of approximately 2 g kg^{-1} and 0.5 °C, respectively, at the base of trade-wind shallow cumulus clouds. It should be noted that they reported temperature measurement errors of approximately 2.6 °C with the Rosemount probe used. Furthermore, the World Meteorological Organization (WMO) recommendations specify minimum useful 1-sigma thresholds of 0.5 g kg^{-1} for WVMR and 0.5 °C for temperature measurements.

Although not all scales of atmospheric variability are accessible to the A–WALI lidar, it is therefore reasonable to adopt RMS error thresholds of 0.5 g kg^{-1} for WVMR and 0.5 °C for temperature to define a theoretical measurement range for each integration time (dash lines in Figure 8). Figure 9 shows the evolution of the lidar measurement range as a function of aerosol loading characterized by the AEC, under nighttime conditions. For WVMR measurements, the range remains on the order of 2-3 km for an integration time of 2 s. It increases substantially for an integration time of 15 s, exceeding 4 km under most conditions. An AEC of 0.2 km^{-1} reduces the measurement range by approximately 30–40% compared with aerosol-free conditions. In contrast, the measurement range remains more limited for temperature retrievals, at less than 0.5 km for a 2-s integration time. This is explained by the much lower noise levels required to meet the 0.5 °C threshold, which corresponds to a small relative error of approximately 2‰. For water vapor, the corresponding relative error is several percent and therefore represents a less stringent requirement, even though the H_2O–Raman channel exhibits a lower signal level.

https://doi.org/10.5194/egusphere-2026-6720
Preprint. Discussion started: 5 November 2026
© Author(s) 2026. CC BY 4.0 License.

More generally, when the signals are affected by Gaussian noise and the RMS of the denominator increases with distance, their ratio may not only become more dispersed but may also exhibit an increasing apparent bias. This effect remains small for WVMR, with a bias below 0.05 g kg^{-1} at a distance of 2 km (Figure 8a), but is more pronounced for temperature retrievals, for which the bias reaches approximately 0.2 °C at 2 km for a 2–s integration time (Figure 8b).

Based on this error budget, the A–WALI lidar can partially meet the scientific requirements for airborne water vapor measurements with an integration time of 2 s, but not for temperature retrievals. An integration time of at least 15 s is required, resulting in a degradation of the horizontal resolution along the aircraft flight path from 0.2 to 1.5 km.

https://doi.org/10.5194/egusphere-2026-6720
Preprint. Discussion started: 5 November 2026
© Author(s) 2026. CC BY 4.0 License.

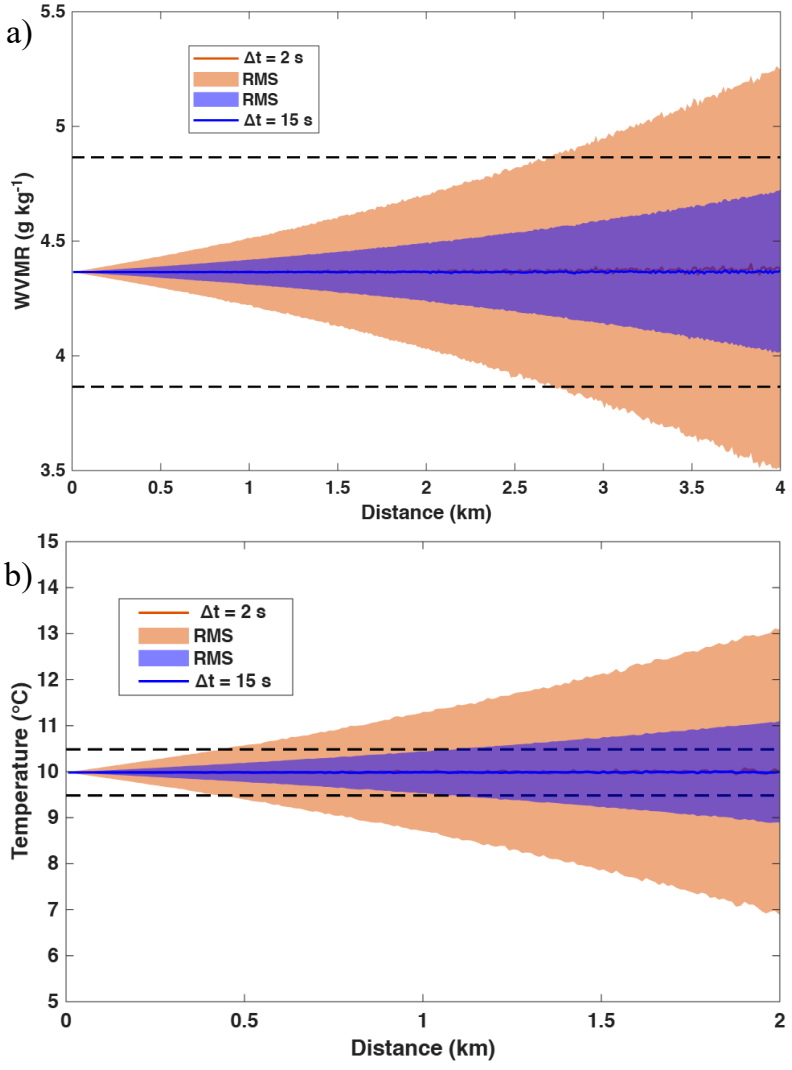


Figure 8. Evolution of the standard deviation as a function of distance from the aircraft for a) a water vapor mixing ratio (WVMR) of 3.9 g kg⁻¹ and b) a temperature of approximately 6 °C. The orange shaded area represents the RMS for an integration time of Δt = 2 s, while the blue shaded area represents the RMS for an integration time of Δt = 15 s. The WMO requirements are indicated by the dashed lines. The range resolution is set to 0.1 km, and the aerosol extinction coefficient is assumed to be 0.1 km⁻¹.

https://doi.org/10.5194/egusphere-2026-6720
Preprint. Discussion started: 5 November 2026
© Author(s) 2026. CC BY 4.0 License.

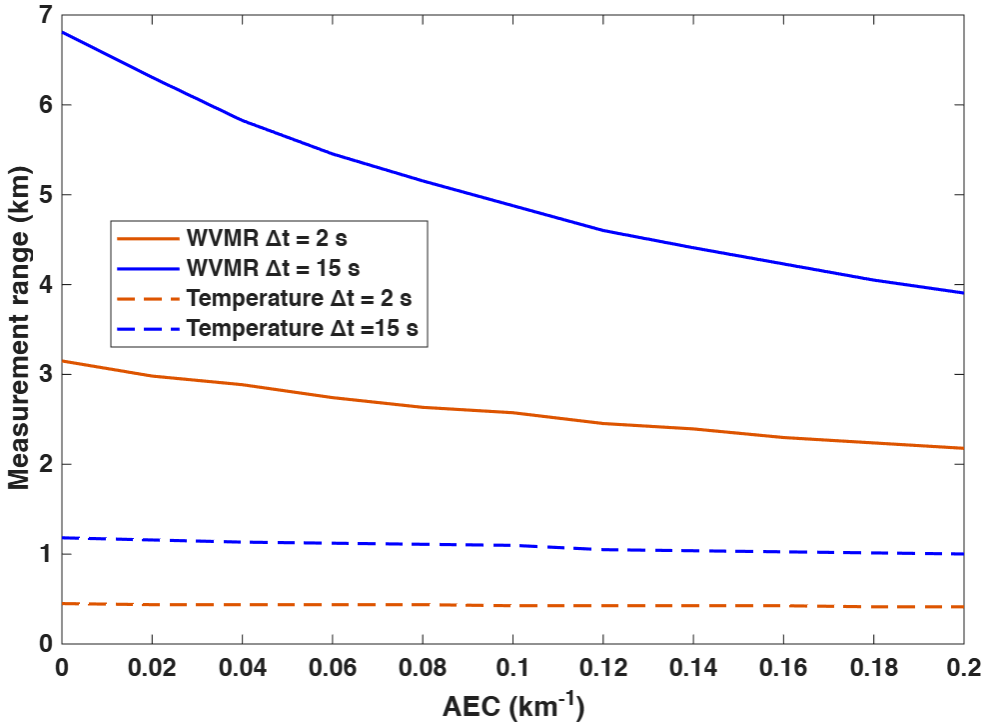


Figure 9. A–WALI measurement range as a function of the aerosol extinction coefficient (AEC) for water vapor mixing ratio (WVMR) and temperature retrievals, using integration times Δt of 2 and 15 s. The range resolution is set to 0.1 km.

4 Application

4.1 Airborne horizontal measurements

Calibration parameters may vary from one flight to another. These changes mainly arise from two sources: mechanical shocks during landing, which can induce a displacement of the telescope mirror, and temperature variations inside the aircraft. Mechanical shocks primarily affect the lidar geometrical overlap factor, whereas temperature variations mainly affect the calibration coefficients for water vapor and temperature retrievals. It should be noted that the angular sensitivity to misalignment of a reflective telescope is several times greater than that of a refractive telescope of the same numerical aperture. This consideration led us in the past to develop lidar systems based on refractive optics (e.g. Chazette et al., 2020). However, the use of Raman channels introduces an additional constraint of maintaining achromatic performance.

To illustrate the airborne measurements already performed with the A-WALI lidar, one of the flights conducted during the MAESTRO campaign is presented here. Flight 15 was performed on 27 August 2024 between 19:00 and 22:30 UTC. Its flight path is shown in Figure 10 using the ASR derived from the elastic channel, with a temporal resolution of 2 s and a range

https://doi.org/10.5194/egusphere-2026-6720
Preprint. Discussion started: 5 November 2026
© Author(s) 2026. CC BY 4.0 License.

resolution of 12 m. All data are shown in this figure without filtering. The aircraft took off from Sal Island (Cabo Verde) and flew within the marine boundary layer at approximately 0.14 km above mean sea level (a.m.s.l.). It then climbed to an altitude of approximately 0.6 km a.m.s.l. to sample the base of a shallow cumulus cloud field. It should be noted that the shallow cumulus cloud field was sampled during two successive flight legs in opposite directions to cover a larger spatial extent. Before landing, the ATR-42 ascended in a spiral pattern to sample the free troposphere above the aerosol layers at approximately 7 km a.m.s.l.

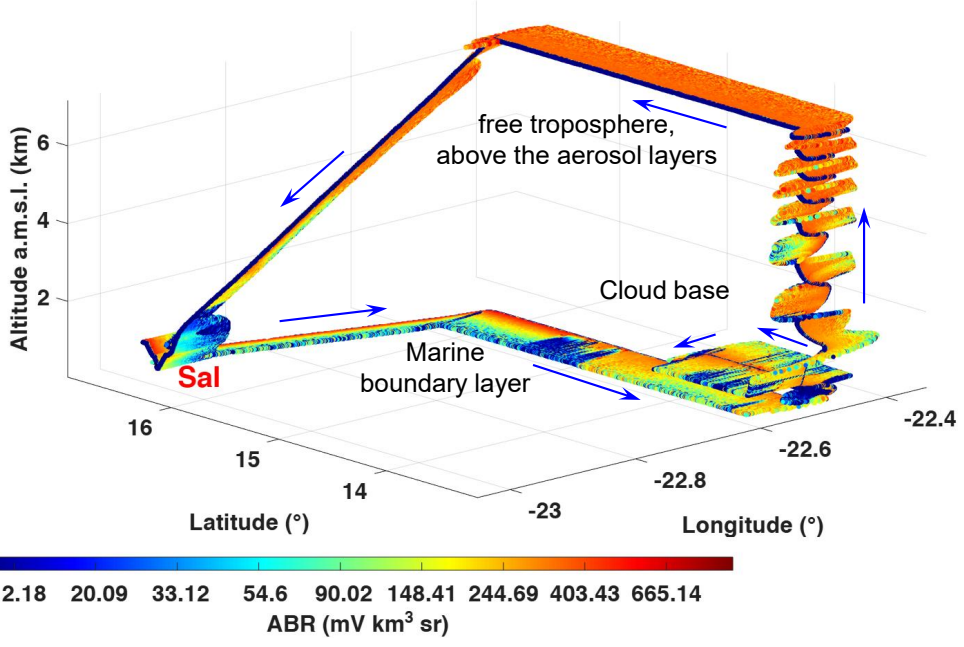


Figure 10. 3D view of the apparent scattering ratio (ASR) derived from the elastic channel along the flight path on 17 August 2024. The blue arrows indicate the direction of flight.

4.1.1 Overlap function

The overlap function was derived directly from the horizontal lidar profiles acquired during Flight 15 and is shown in Figure 11. It is representative of all lidar channels, with the variability among channels indicated by the shaded area in the figure. The overlap function reaches unity at distances greater than 0.28 km from the aircraft. At shorter distances, the measurements are corrected for incomplete overlap, and this correction does not introduce significant errors at distances greater than 0.2 km. As previously mentioned, this function must be reassessed for each flight.

https://doi.org/10.5194/egusphere-2026-6720
Preprint. Discussion started: 5 November 2026
© Author(s) 2026. CC BY 4.0 License.

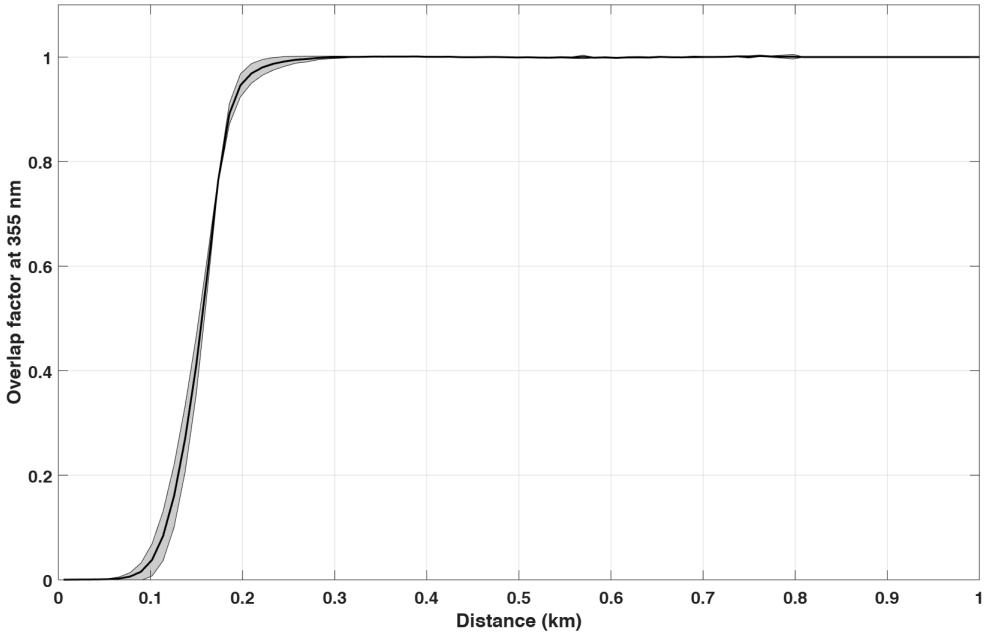


Figure 11. Overlap factor derived for Flight 15 on 27 August 2024.

4.1.2 Aerosols

The vertical AEC profile is retrieved using Eq. (3) over a range of 0.4 to 1 km from the aircraft (Figure 12a). The retrieval is performed at 355 nm using both the elastic channel and the combined RR1–RR2 rotational Raman channel, the latter being insensitive to temperature variations. Very good agreement is observed between the two retrievals, demonstrating the robustness of the approach. The standard deviations, represented by the shaded areas in the figure, are similar for both retrievals, with values of approximately 0.02 km^{-1}. This value is higher than that obtained from the simulations, as it also includes the natural variability of aerosol optical properties at each altitude level. It is similar to that obtained during the EUREC4A airborne campaign (Chazette et al., 2022).

Most of the aerosols sampled during the flight are of Saharan origin, as shown in Figure 12b, which combines Terra/MODIS and Aqua/MODIS observations (King et al., 1992; Salomonson et al., 1989) with SEVIRI observations over the ocean (Bennouna et al., 2009). The geographical area covered by the flight is also indicated in the figure. The AOT at 550 nm is approximately 0.3 in this region, close to the value derived from the lidar measurements by integrating the vertical AEC profile (Eq. 2), 0.31 in Figure 12a.

https://doi.org/10.5194/egusphere-2026-6720
Preprint. Discussion started: 5 November 2026
© Author(s) 2026. CC BY 4.0 License.

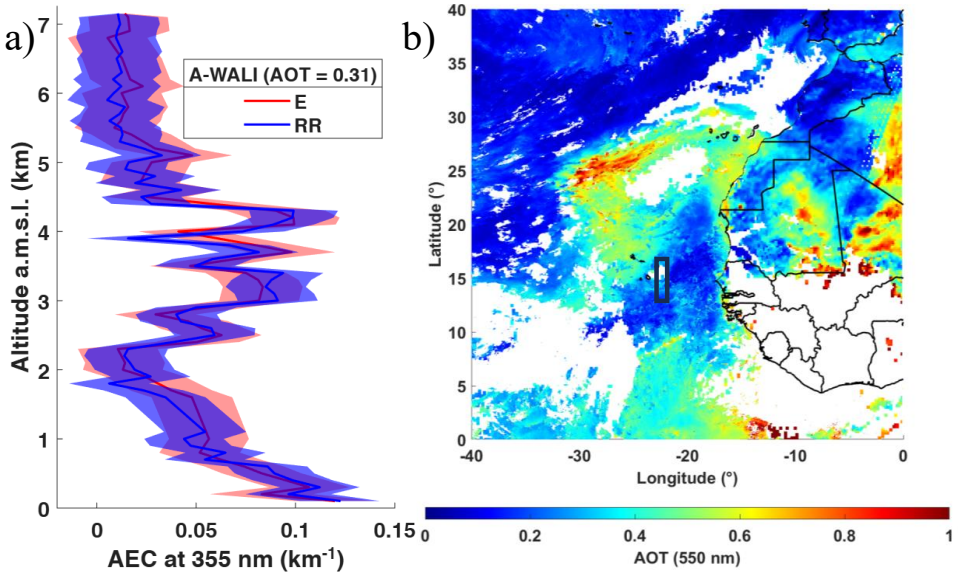


Figure 12. a) Lidar-derived vertical profiles of the mean aerosol extinction coefficient (AEC), with the corresponding root mean square (RMS) variability indicated by the shaded areas, for Flight 15 on 27 August 2024. The elastic (E) and rotational Raman (RR) channels are considered. b) Composite image of the aerosol optical thickness (AOT) at 550 nm derived from MODIS observations over land and SEVIRI observations over the ocean.

4.1.3 Cloud horizontal structures

The method used is described in Chazette et al. (2020) and was applied to the horizontal profiles at their native temporal resolution and with a range resolution of 12 m. It was developed following the EUREC^{4}A airborne campaign to determine cloud-base dimensions along the lidar line of sight. A shallow cumulus cloud field is present along part of the flight leg at the aircraft altitude of 0.6 km. The unfolded view of this flight leg is shown in Figure 13a, with clouds appearing in brown. Figure 13b presents the results of the data analysis.

Cloud-base dimensions are generally on the order of a few hundred meters, as previously observed during EUREC^{4}A. The horizontal structure of the cloud field appears consistent between Figure 13a and b. The statistical distribution of cloud dimensions along the lidar line of sight is shown in Figure 14. Two analysis ranges were considered to assess the consistency of the method. For a homogeneous cloud field, the probability distribution functions (PDF) obtained over the two ranges are expected to be similar. They are indeed very close to each other, consistent with previous observations for the same type of broken cloud cover during EUREC^{4}A.

https://doi.org/10.5194/egusphere-2026-6720
Preprint. Discussion started: 5 November 2026
© Author(s) 2026. CC BY 4.0 License.

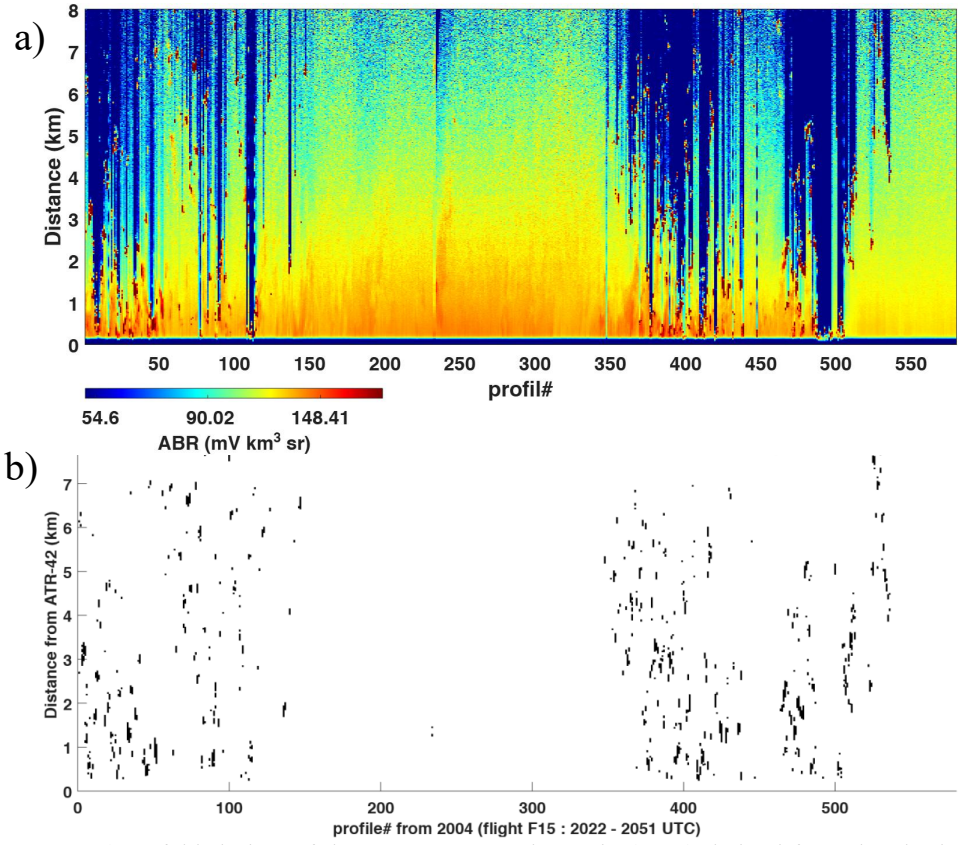


Figure 13. a) Unfolded view of the apparent scattering ratio (ASR) derived from the elastic channel at a flight altitude of 0.6 km for Flight 15 on 17 August 2024. b) Cloud detection derived from A-WALI measurements along the horizontal line of sight.

https://doi.org/10.5194/egusphere-2026-6720
Preprint. Discussion started: 5 November 2026
© Author(s) 2026. CC BY 4.0 License.

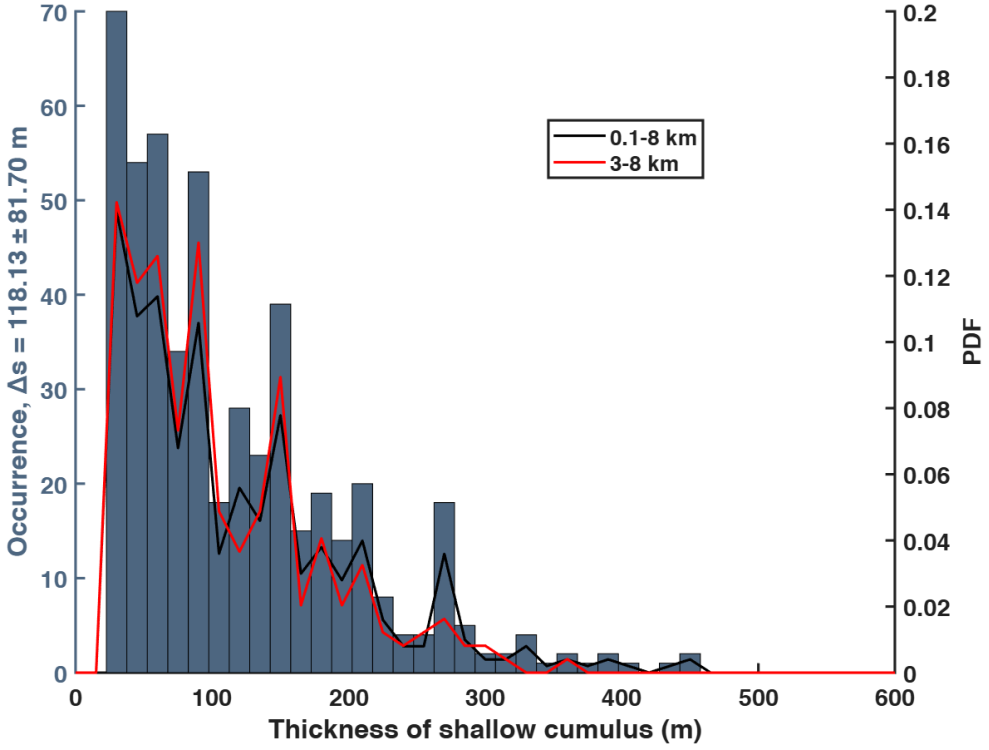


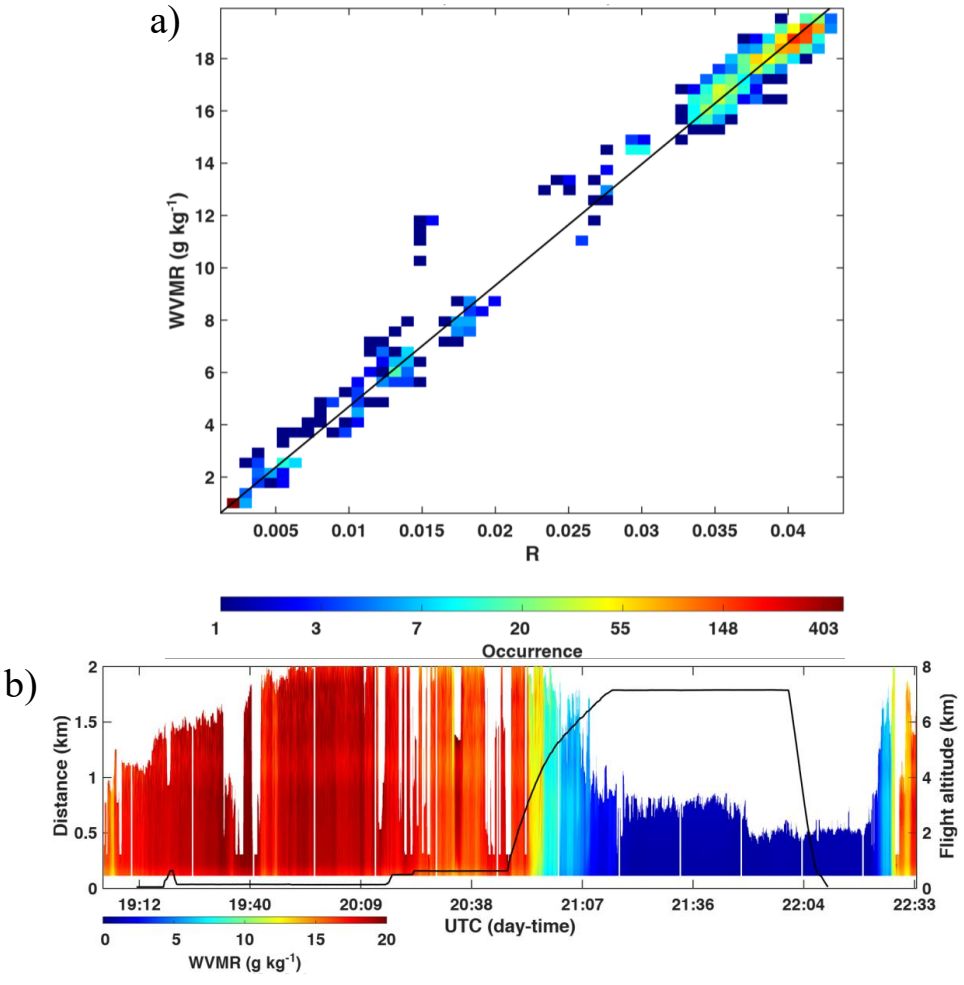
Figure 14. Number of clouds detected along the horizontal line of sight of the lidar that correspond to different cloud widths during flight F15 on 17 August 2024. Also reported (right-hand side vertical axis) is the probability distribution function (PDF) of cloud widths for the clouds detected at horizontal distances from the aircraft ranging from 0.1 and 8 km (black solid line) and from 3 to 8 km (red solid line).

4.1.4 Water vapor

The first step consists of correcting each channel for the overlap factor, temperature dependence (Figure 5), molecular transmission, and particulate transmission to derive the ratio $R(x,z)$ (Eq. 6). Then, for each horizontal profile, the mean value of $R(x,z)$ is calculated over the [0.25–0.5] km range interval. For calibration purpose, it is compared with in situ meteorological measurements performed aboard the aircraft using a WVSS–II probe (SpectraSensors). This comparison assumes that the water vapor mixing ratio remains constant over the selected range interval. The calibration results are shown in Figure 15a. The regression correlation coefficient is ~0.99, and the residual calibration-related difference between the lidar and airborne in situ measurements is 0.45 g kg^{-1}. It should be noted that the aircraft's ascent and descent rates may introduce additional scatter in the measurements, which is difficult to quantify and is therefore accounted for in the residual calibration differences.

https://doi.org/10.5194/egusphere-2026-6720
Preprint. Discussion started: 5 November 2026
© Author(s) 2026. CC BY 4.0 License.

Figure 15b shows the retrieved WVMR field for a 2-s integration time and a range resolution of 100 m. As shown by the sensitivity analysis, the measurement range does not exceed approximately 0.6–1.5 km in the lower atmospheric layers, where the AEC ranges between 0.05 and 0.1 km^{-1}. The measurement range is also very limited at higher altitudes because of the low water vapor content around 7 km a.m.s.l. (WVMR < 1 g kg^{-1}). The white areas in the figure indicate regions where the signal-to-noise ratio of the H_2O Raman channel ASR is below 5 or where the aircraft tilt exceeds 5°. Data significantly affected by clouds are excluded. It should be noted that aeronautical night begins at approximately 20:30 UTC, and that the measurements acquired before this time are affected by sky background radiance. The gradual decrease in sky background radiance during the flight accounts for the increase in lidar measurement range observed in the lower troposphere, at altitudes below 0.3 km a.m.s.l.



https://doi.org/10.5194/egusphere-2026-6720
Preprint. Discussion started: 5 November 2026
© Author(s) 2026. CC BY 4.0 License.

Figure 15. a) Calibration curve of A–WALI water vapor mixing ratio (WVMR) measurements against the WVSS-II probe ($r_{H_2O}(x,z) = 463.6 \cdot R(x,z) + 0.059$). b) Lidar-derived WVMR with a range resolution of 100 m during Flight 15 on 17 August 2024.

4.1.5 Temperature

The calibration used to retrieve temperature from the airborne lidar measurements follows the same approach as that used for water vapor, based on Eqs. (9) and (10), but using measurements from a Rosemount PT102E2AL probe as the in situ reference. As shown in Figure 16a, the calibration relationship is effectively linear over the temperature range sampled during the flight, with a residual calibration-related difference of 0.69 °C between the lidar and the in situ measurements. Excluding measurements exhibiting a dispersion greater than one standard deviation helps mitigate the effect of lidar inclination, as an inclination of 5° leads to a temperature bias of approximately 1.1 °C at a range of 2 km. It is worth noting that the observed angular variability of the aircraft during straight and level flight legs ranged between 1.5° and 2°.

The temperature field retrieved from the lidar measurements is shown in Figure 16b. Beyond approximately 0.5 km from the aircraft, the retrieved field becomes increasingly noisy and spatially fragmented, as expected from the sensitivity analysis. In the lower troposphere, temperature RMS error exceeding 10 °C are observed at distances greater than 2 km from the aircraft, making the measurements unsuitable for investigating the spatial variability of the temperature field between clouds. These results therefore highlight the need for substantial instrumental improvements, which would require major and technically constraining modifications to the airborne platform to achieve the performance required for this type of measurement.

https://doi.org/10.5194/egusphere-2026-6720
Preprint. Discussion started: 5 November 2026
© Author(s) 2026. CC BY 4.0 License.

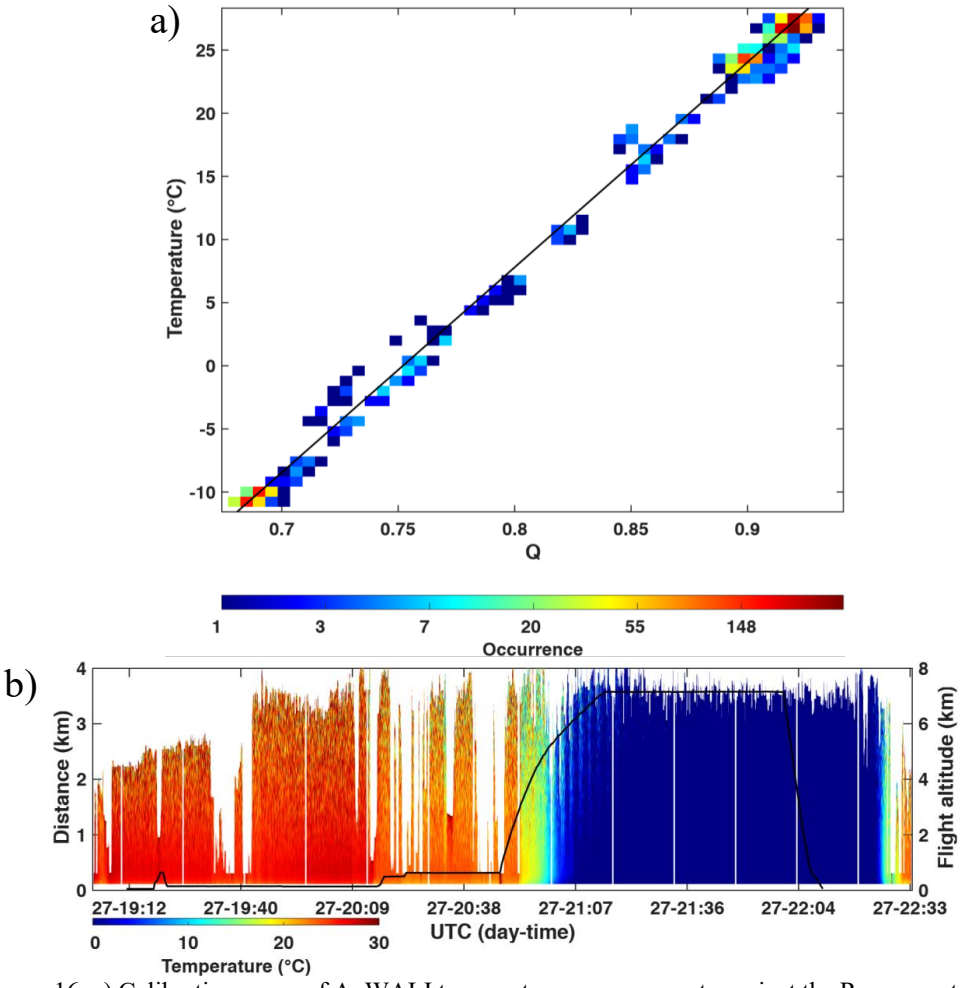


Figure 16. a) Calibration curve of A–WALI temperature measurements against the Rosemount PT102E2AL probe ($T(x,z) = 162.5 \cdot Q(x,z) - 122.2$). b) Lidar-derived temperature with a range resolution of 100 m during Flight 15 on 17 August 2024.

4.2 Ground-based horizontal measurements

Following the MAESTRO airborne campaign, the A-WALI lidar was characterized in the laboratory to assess its performance under controlled environmental conditions, particularly with ambient temperature variations of less than 1 °C. The test period extended from 4 to 7 April 2025, with continuous daytime and nighttime measurements performed from the laboratory located at the CEA Orme des Merisiers site (48.71° N, 2.15° E). An integration time of 15 s was selected.

https://doi.org/10.5194/egusphere-2026-6720
Preprint. Discussion started: 5 November 2026
© Author(s) 2026. CC BY 4.0 License.

4.2.1 Aerosols

Figure 17 shows the temporal evolution of the AEC retrieved from the elastic channel and from the combination of the rotational Raman channels. As for the airborne measurements, very good agreement is observed between these two independent retrievals. The AEC values observed during the test period are similar to those measured during Flight 15 in the lower and middle troposphere. These results therefore demonstrate the reliability of A–WALI for AEC retrievals aboard the ATR–42.

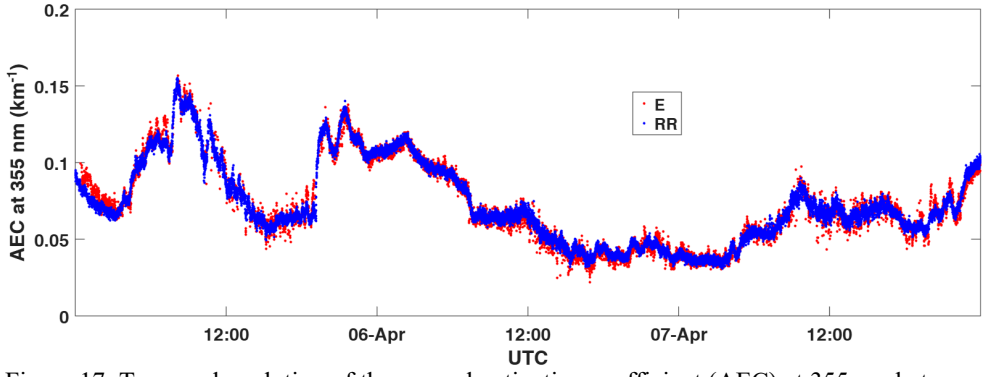


Figure 17. Temporal evolution of the aerosol extinction coefficient (AEC) at 355 nm between 4 and 7 April 2025, as derived from A–WALI horizontal lidar measurements. The elastic (E) and the combination of the rotational Raman (RR) channels are used.

4.2.2 Water vapor

The lidar-derived water vapor product was compared with in situ measurements performed outside the building at the same altitude as the lidar. A Vaisala PTU–300 meteorological probe was installed approximately 1 m from the building. As the building is heated during the daytime, it may locally influence the in situ measurements and contribute to the dispersion of the data points. Figure 18a shows the resulting calibration curve, with a correlation coefficient greater than 0.99. The residual calibration error is 0.082 g kg^{-1}.

Figure 18b shows the temporal evolution of the horizontal WVMR profiles retrieved from the lidar measurements at a range resolution of 100 m. The WVMR exhibits strong temporal variability, with values comparable to those observed during the previously presented flight. The measurement range is consistent with the sensitivity analysis for a 15 s integration time, accounting for the decreasing aerosol loading over time. The PTU–300 measurements agree well with the lidar-derived WVMR at a distance of 0.3 km from the building. Good agreement is also observed at 1 km, although the noise level is substantially higher, particularly during daytime.

https://doi.org/10.5194/egusphere-2026-6720
Preprint. Discussion started: 5 November 2026
© Author(s) 2026. CC BY 4.0 License.

The WVMR derived from ERA5 reanalysis data is also shown in the figure and is in good agreement with the observations. This agreement indicates that the overall variation in water vapor concentration occurs on spatial scales comparable to the ERA5 grid-cell size (~18 × 18 km²). However, significant variability occurring at smaller spatial scales, such as that observed between 5 and 6 April, may be not captured by the reanalysis.

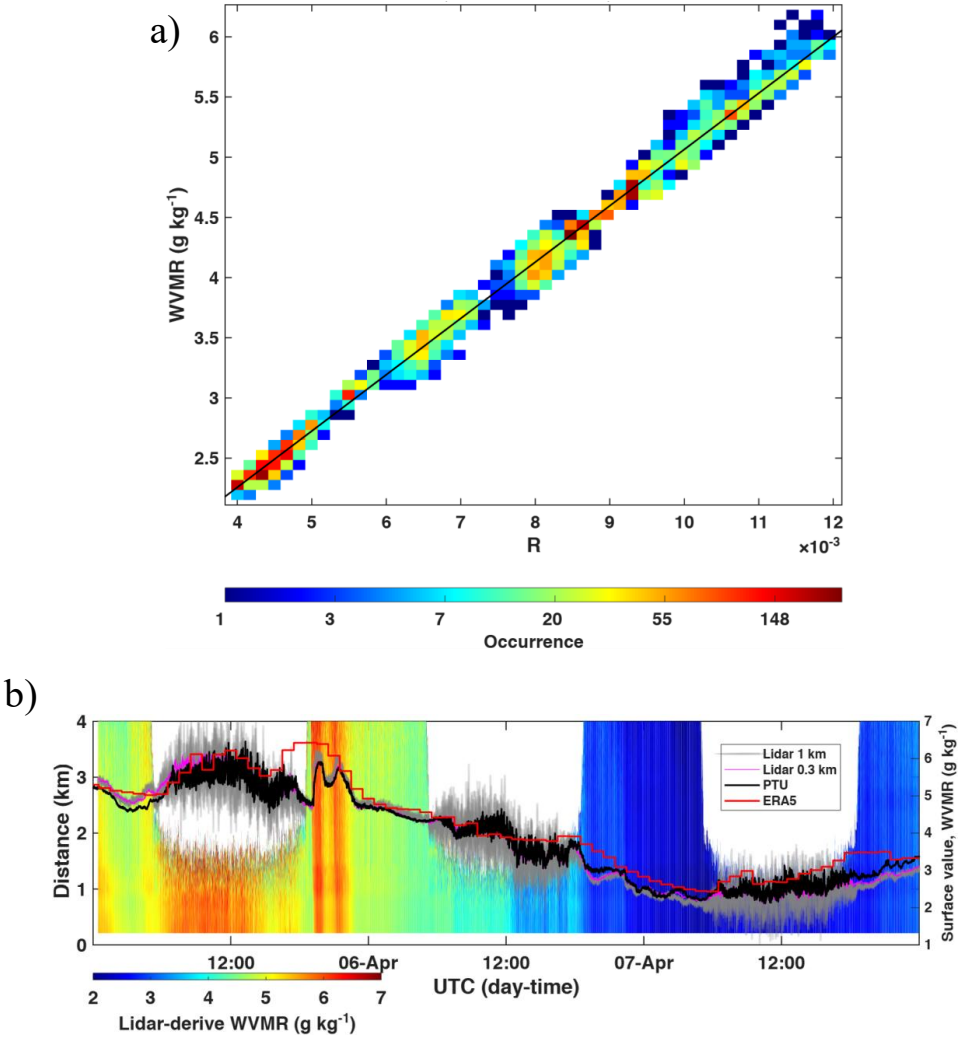


Figure 18. a) Calibration curve of ground-based horizontal temperature measurements by A–WALI against the PTU–300 probe ($r_{H_2O}(x,z) = 499.8 \cdot R(x,z) + 0.16$). b) Lidar-derived WVMR between 4 and 7 April 2025. The temporal evolution of the lidar measurements at distances of 0.3 and 1 km from the building is also presented, together with measurements from the PTU–300 probe and ERA5 reanalysis data from the grid point centred on the measurement site.

https://doi.org/10.5194/egusphere-2026-6720
Preprint. Discussion started: 5 November 2026
© Author(s) 2026. CC BY 4.0 License.

4.2.3 Temperature

As for water vapor, the atmospheric temperature retrieved from the Raman lidar measurements was compared with measurements from the Vaisala PTU–300 meteorological probe. The calibration relationship (Figure 19a) appears nearly linear over the observed temperature range, with a residual calibration error of 0.62 °C and a correlation coefficient of 0.98. The lidar was tilted upward by 3° to avoid obstacles along the line of sight. This inclination corresponds to a temperature decrease of approximately 1.4 °C at a distance of 4 km due to the increase in altitude along the line of sight. Consequently, the atmospheric temperature tends to decrease with increasing distance from the building.

The temporal evolution of the horizontal temperature profiles is shown in Figure 19b. At both 0.3 and 1 km from the building, the temporal evolution of the lidar-derived temperature closely follows that measured by the PTU–300 probe. As expected, the agreement is substantially better during nighttime than during daytime. This difference does not appear to be primarily related to the statistical noise of the lidar measurements, but rather to the daytime influence of the building on the PTU–300 measurements. At a distance of 1 km, the RMS error exceeds the 0.5 °C threshold but remains below 1 °C.

https://doi.org/10.5194/egusphere-2026-6720
Preprint. Discussion started: 5 November 2026
© Author(s) 2026. CC BY 4.0 License.

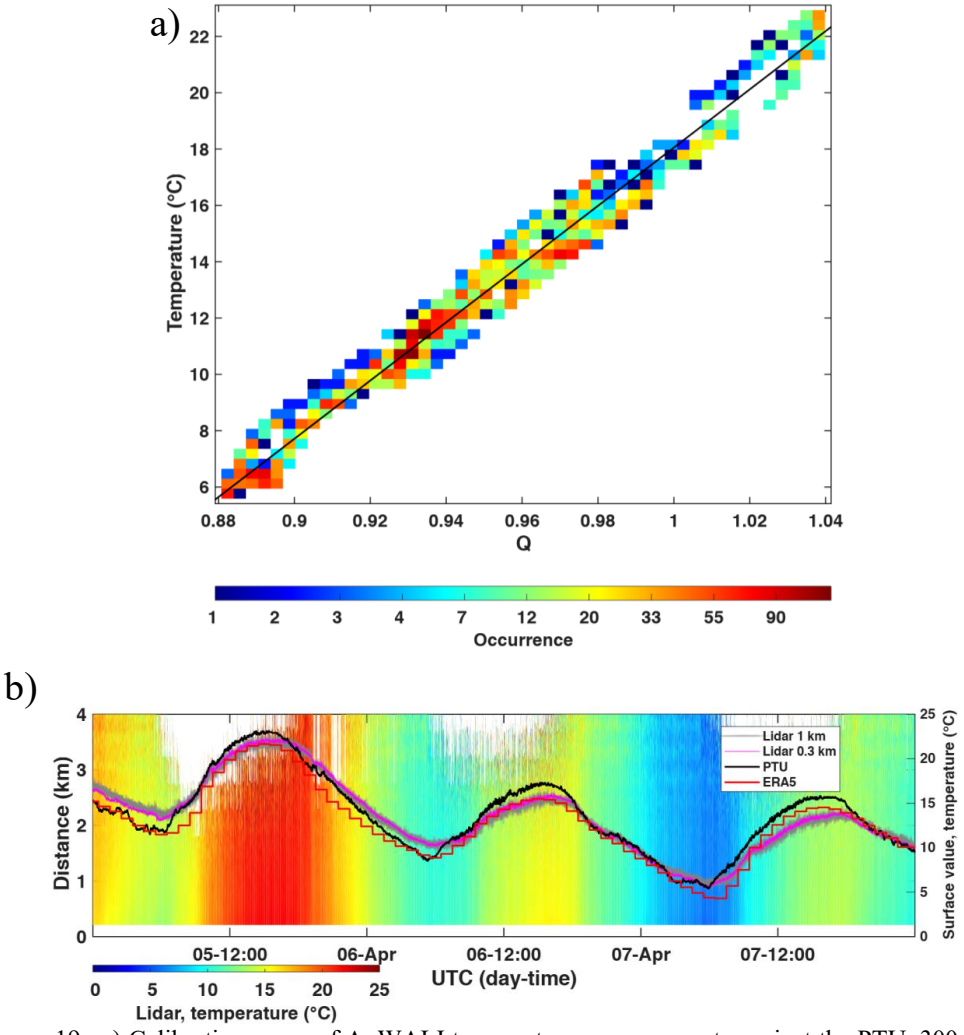


Figure 19. a) Calibration curve of A–WALI temperature measurements against the PTU–300 probe ($T(x,z) = 103.1 \cdot Q(x,z) - 84.95$). b) Lidar-derived temperature between 4 and 7 April 2025. The temporal evolution of the lidar measurements at distances of 0.3 and 1 km from the building is also presented, together with measurements from the PTU–300 probe and ERA5 reanalysis data from the grid point centered on the measurement site.

4.2.4 Consistency with zenith measurements

Water vapor and temperature lidar measurements are commonly performed from the ground using a zenith-pointing configuration. This section discusses measurements performed with A–WALI in this configuration. As in Chazette et al. (2025), the lidar profiles were averaged over ±15 min around the launch time of the radiosonde from the Météo-France station at Trappes. The measurements were acquired during the night of 24–25 April 2026 and provide a clearer

https://doi.org/10.5194/egusphere-2026-6720
Preprint. Discussion started: 5 November 2026
© Author(s) 2026. CC BY 4.0 License.

assessment of the ability of A–WALI to retrieve vertical profiles of water vapor and temperature. The averaging was performed over 360,000 individual profile samples.

As shown in Figure 20, the meteorological profiles retrieved from the lidar measurements are in very good agreement with the radiosonde measurements. Differences in WVMR are observed below 1 km a.m.s.l., most likely due to the geographical separation between the lidar and radiosonde stations, which are approximately 14 km apart. In the free troposphere, the difference remains below 0.5 g kg^{-1}. The mean differences between the temperature profiles retrieved from the lidar and radiosonde measurements generally remain below 0.5 °C. The RMS error increases with altitude, reaching values between 2 and 3 °C at approximately 7 km a.m.s.l.

These results demonstrate that the lidar system itself is suitable for retrieving water vapor and temperature profiles in both zenith-pointing and horizontal configurations. Its performance aboard the aircraft is therefore primarily limited by the much shorter integration times imposed by airborne measurements.

The profiles derived from ERA5 reanalysis data are also shown in Figure 20. The agreement is relatively poor for WVMR but very good for temperature. This result provides further evidence, consistent with Chazette et al. (2026), that the deployment of a lidar network could make a significant contribution to improving weather forecasts.

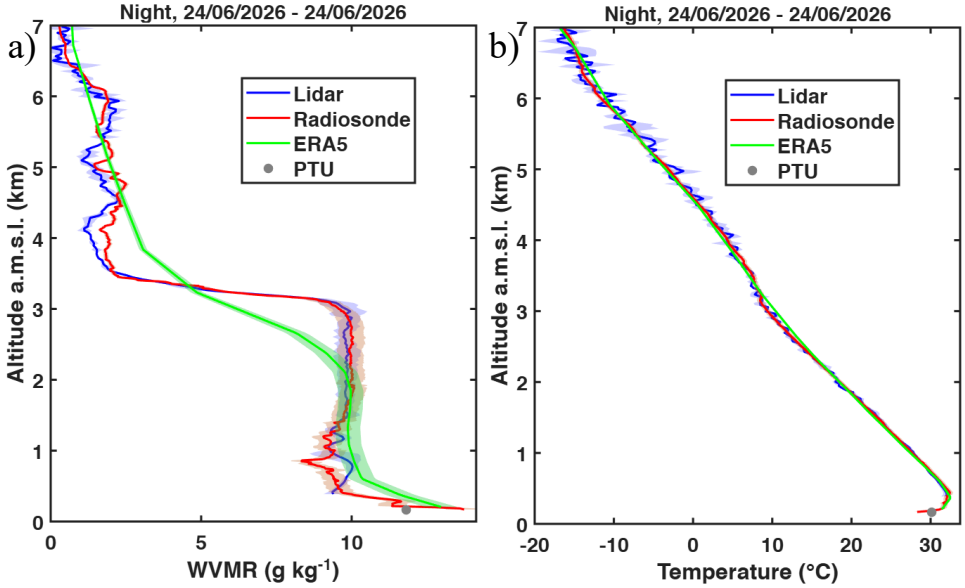


Figure 20. Vertical profiles of (a) water vapor mixing ratio (WVMR) and (b) temperature derived from A–WALI, radiosonde measurements, and ERA5 reanalysis data. The measurement from the PTU–300 probe is also shown in grey.

https://doi.org/10.5194/egusphere-2026-6720
Preprint. Discussion started: 5 November 2026
© Author(s) 2026. CC BY 4.0 License.

5 Conclusion on A–WALI performance, limitations, and perspectives

The A–WALI Raman lidar was specifically developed to perform measurements during the MAESTRO airborne campaign conducted off the coast of Cabo Verde. This side-looking remote-sensing instrument provides the capability to sample horizontal fields of clouds, aerosols, water vapor, and temperature. Its design was strongly constrained by the requirements associated with airborne measurements through a side window of the aircraft. The laser power is limited to comply with eye-safety requirements, whereas the telescope diameter is constrained by the size of the side window, which is comparable to that of a conventional aircraft window. The number of profiles that can be averaged is also limited by the spatial scales of the atmospheric structures to be investigated. For an aircraft cruising at approximately 100 m s^{-1} and a laser repetition rate of 200 Hz, an integration time of 2 s and a range resolution of 100 m were selected. The integration time can be increased to 15 s for investigations at larger spatial scales, corresponding to a resolution of approximately 1.5 km along the aircraft flight path.

Together, these constraints result in a severe limitation of the signal-to-noise ratio, particularly for the Raman channels. Aerosol optical properties and the horizontal dimensions of semi-transparent cloud structures can be retrieved at distances of up to approximately 8 km. At night, the measurement range for WVMR retrievals, considering an RMS error threshold of 0.5 g kg^{-1}, is approximately 2.5–3 km for a 2-s integration time and 4–5 km for a 15-s integration time. The corresponding ranges are substantially shorter for temperature retrievals, reaching only approximately 0.4–0.5 km and 1.1–1.2 km for integration times of 2 and 15 s, respectively, considering an RMS error threshold of 0.5 °C. These performances are strongly degraded during daytime because of the increased sky background radiance, making Raman measurements of water vapor and temperature difficult to exploit for investigating heterogeneities between cloud structures, particularly with a 2-s integration time.

In practice, there are few possibilities for substantially improving the system while complying with the constraints imposed by aircraft safety requirements and aircraft geometry. A larger telescope could be considered, but this would require either the installation of a dedicated side window or the use of a periscope mounted on the underside of the aircraft or within an external pod. Such modifications would be extremely costly and would require extensive aeronautical certification. Assuming a telescope diameter of 50 cm, the signal-to-noise ratio could be improved by a factor of approximately 3.3, resulting in a improvement of the nighttime measurement range by a similar factor. However, the use of a larger telescope would adversely

https://doi.org/10.5194/egusphere-2026-6720
Preprint. Discussion started: 5 November 2026
© Author(s) 2026. CC BY 4.0 License.

affect the overlap function at short ranges and could therefore reduce the quality of the calibration.

Finally, the quality and stability of the aerosol extinction coefficient measurements suggest that A–WALI observations could be used to validate aerosol optical products from the EarthCARE satellite mission. Several EarthCARE overpasses intersected the aircraft flight path during the campaign, providing potentially valuable opportunities for such validation.

Data availability. The A–WALI airborne datasets are published and openly available through the AERIS database at DOI: 10.25326/886. The ERA5 products are available at https://cds.climate.copernicus.eu/datasets (last access: 18 September 2026).

Author contributions. PC and JT jointly developed the conceptual design of the lidar system. PC participated in the field campaign, developed the retrieval algorithms, performed the data analysis, and wrote the manuscript. JT built the lidar system and reviewed the manuscript.

Competing interests. The authors declare that they have no conflict of interest.

Acknowledgments. The authors gratefully acknowledge Sandrine Bony for coordinating the MAESTRO field campaign and supporting the development of the A–WALI lidar through her European Research Council (ERC) grant. Special thanks are extended to the SAFIRE team and the LSCE lidar team, particularly Jérémy Lagarrigue, Frédéric Laly, Laurent Forges, Valentin Guillet, and Hélène Cassan, for their contributions to the acquisition of the airborne data used in this study. The authors also acknowledge the Copernicus Climate Change Service (C3S) for providing ERA5 reanalysis data through the Climate Data Store (CDS), and Météo-France for providing access to radiosonde observations from the Trappes station.

Financial support. CEA/DRF and CNRS/INSU also contributed to the funding of this work by providing resources and personnel. This research received funding from ERC MAESTRO Advanced grant no. 101098063.

6 References

Adam, M.: Notes on temperature-dependent lidar equations, J. Atmos. Ocean. Technol., 26, 1021–1039, https://doi.org/10.1175/2008JTECHA1206.1, 2009.

Avila, G., Fernández, J. M., Tejeda, G., and Montero, S.: The Raman spectra and cross-sections of H2O, D2O, and HDO in the OH/OD stretching regions, J. Mol. Spectrosc., 228, 38–65, https://doi.org/10.1016/j.jms.2004.06.012, 2004.

Behrendt, A.: Temperature Measurements with Lidar, in: Lidar: Range-Resolved Optical Remote Sensing of the Atmosphere, Springer-Verlag, New York, 273–305, https://doi.org/10.1007/0-387-25101-4_10, 2006.

Bony, S., Stevens, B., Ament, F., Bigorre, S., Chazette, P., Crewell, S., Delanoë, J., Emanuel, K., Farrell, D., Flamant, C., Gross, S., Hirsch, L., Karstensen, J., Mayer, B., Nuijens, L.,

https://doi.org/10.5194/egusphere-2026-6720
Preprint. Discussion started: 5 November 2026
© Author(s) 2026. CC BY 4.0 License.

Ruppert, J. H., Sandu, I., Siebesma, P., Speich, S., Szczap, F., Totems, J., Vogel, R., Wendisch, M., and Wirth, M.: EUREC4A: A Field Campaign to Elucidate the Couplings Between Clouds, Convection and Circulation, Surv. Geophys., 38, 1529–1568, https://doi.org/10.1007/s10712-017-9428-0, 2017.

Bony, S., Lothon, M., Delanoë, J., Coutris, P., Etienne, J. C., Aemisegger, F., Albright, A. L., André, T., Bellec, H., Baron, A., Bourdinot, J. F., Brilouet, P. E., Bourdon, A., Canonici, J. C., Caudoux, C., Chazette, P., Cluzeau, M., Cornet, C., Desbios, J. P., Duchanoy, D., Flamant, C., Fildier, B., Gourbeyre, C., Guiraud, L., Jiang, T., Lainard, C., Le Gac, C., Lendroit, C., Lernould, J., Perrin, T., Pouvesle, F., Richard, P., Rochetin, N., Salaün, K., Schwarzenboeck, A., Seurat, G., Stevens, B., Totems, J., Touzé-Peiffer, L., Vergez, G., Vial, J., Villiger, L., and Vogel, R.: EUREC4A observations from the SAFIRE ATR42 aircraft, Earth Syst. Sci. Data, 14, 2021–2064, https://doi.org/10.5194/essd-14-2021-2022, 2022.

Brilouet, P. E., Lothon, M., Etienne, J. C., Richard, P., Bony, S., Lernoult, J., Bellec, H., Vergez, G., Perrin, T., Delanoë, J., Jiang, T., Pouvesle, F., Lainard, C., Cluzeau, M., Guiraud, L., Medina, P., and Charoy, T.: The EUREC4A turbulence dataset derived from the SAFIRE ATR 42 aircraft, Earth Syst. Sci. Data, 13, 3379–3398, https://doi.org/10.5194/essd-13-3379-2021, 2021.

Bruneau, D., Quaglia, P., Flamant, C., Meissonnier, M., and Pelon, J.: Airborne Lidar LEANDRE II for Water-Vapor Profiling in the Troposphere. I. System description., Appl. Opt., 40, 3450–3461, 2001.

Bruneau, D., Pelon, J., Blouzon, F., Spatazza, J., Genau, P., Buchholtz, G., Amarouche, N., Abchiche, A., and Aouji, O.: 355-nm high spectral resolution airborne lidar LNG: system description and first results, Appl. Opt., 54, 8776, https://doi.org/10.1364/ao.54.008776, 2015.

Burton, S. P., Ferrare, R. A., Hostetler, C. A., Hair, J. W., Rogers, R. R., Obland, M. D., Butler, C. F., Cook, A. L., Harper, D. B., and Froyd, K. D.: Aerosol classification using airborne High Spectral Resolution Lidar measurements – methodology and examples, Atmos. Meas. Tech., 5, 73–98, https://doi.org/10.5194/amt-5-73-2012, 2012.

Chazette, P., Pelon, J., Moulin, C., Dulac, F., Carrasco, I., Guelle, W., Bousquet, P., and Flamant, P.-H.: Lidar and satellite retrieval of dust aerosols over the Azores during SOFIA/ASTEX, Atmos. Environ., 35, 4297–4304, https://doi.org/10.1016/S1352-2310(01)00253-9, 2001.

Chazette, P., Randriamiarisoa, H., Sanak, J., Couvert, P., and Flamant, C.: Optical properties of urban aerosol from airborne and ground-based in situ measurements performed during the Etude et Simulation de la Qualité de l'air en Ile de France (ESQUIF) program, J. Geophys. Res., 110, D02206, https://doi.org/10.1029/2004JD004810, 2005.

Chazette, P., Dabas, A., Sanak, J., Lardier, M., and Royer, P.: French airborne lidar measurements for Eyjafjallajökull ash plume survey, Atmos. Chem. Phys., 12, 7059–7072, https://doi.org/10.5194/acp-12-7059-2012, 2012.

Chazette, P., Flamant, C., Totems, J., Gaetani, M., Smith, G., Baron, A., Landsheere, X., Desboeufs, K., Doussin, J. F., and Formenti, P.: Evidence of the complexity of aerosol transport in the lower troposphere on the Namibian coast during AEROCLO-sA, Atmos. Chem. Phys., 19, 14979–15005, https://doi.org/10.5194/acp-19-14979-2019, 2019.

Chazette, P., Totems, J., Baron, A., Flamant, C., and Bony, S.: Trade-wind clouds and aerosols characterized by airborne horizontal lidar measurements during the EUREC4A field campaign, Earth Syst. Sci. Data, 12, 2919–2936, https://doi.org/10.5194/essd-12-2919-2020, 2020.

Chazette, P., Flamant, C., Sodemann, H., Totems, J., Monod, A., Dieudonné, E., Baron, A., Seidl, A., Steen-Larsen, H. C., Doira, P., Durand, A., and Ravier, S.: Experimental investigation of the stable water isotope distribution in an Alpine lake environment (L-

https://doi.org/10.5194/egusphere-2026-6720
Preprint. Discussion started: 5 November 2026
© Author(s) 2026. CC BY 4.0 License.

WAIVE), Atmos. Chem. Phys., 21, 10911–10937, https://doi.org/10.5194/acp-21-10911-2021, 2021.

Chazette, P., Baron, A., and Flamant, C.: Mesoscale spatio-temporal variability of airborne lidar-derived aerosol properties in the Barbados region during EUREC4A, Atmos. Chem. Phys., 22, 1271–1292, https://doi.org/10.5194/acp-22-1271-2022, 2022.

Chazette, P., Totems, J., and Laly, F.: Long-term evolution of the calibration constant on a mobile water vapour Raman lidar, Atmos. Meas. Tech., 18, 2681–2699, https://doi.org/10.5194/amt-18-2681-2025, 2025.

Chazette, P., Behrendt, A., Comerón, A., Girolamo, P. Di, Paolantonio, M. Di, Dionisi, D., Flamant, C., Gómez-amo, J. L., Lagarrigue, J., Laly, F., and Lange, D.: To what extent are the IASI and ERA5 water vapour profiles representative of the conditions in the autumn 2022 during the WaLiNeAs field campaign, Atmos. Meas. Tech., 1, 5223–5242, https://doi.org/https://doi.org/10.5194/amt-19-5223-2026, 2026.

Dulac, F. and Chazette, P.: Airborne study of a multi-layer aerosol structure in the eastern Mediterranean observed with the airborne polarized lidar ALEX during a STAAARTE campaign (7 June 1997), Atmos. Chem. Phys., 3, 1817–1831, https://doi.org/10.5194/acp-3-1817-2003, 2003.

Flamant, C., Gaetani, M., Chaboureau, J. P., Chazette, P., Cuesta, J., Piketh, S. J., and Formenti, P.: Smoke in the river: an Aerosols, Radiation and Clouds in southern Africa (AEROCLO-sA) case study, Atmos. Chem. Phys., 22, 5701–5724, https://doi.org/10.5194/acp-22-5701-2022, 2022.

Gerasimov, V. V. and Zuev, V. V.: Analytical calibration functions for the pure rotational Raman lidar technique, Opt. Express, 24, 5136, https://doi.org/10.1364/oe.24.005136, 2016.

Heaps, W. S. and Burris, J.: Airborne Raman lidar, Appl. Opt., 35, 7128, https://doi.org/10.1364/ao.35.007128, 1996.

Hogan, R. J., Francis, P. N., Flentje, H., Illingworth, A. J., Quante, M., and Pelon, J.: Characteristics of mixed-phase clouds. I: Lidar, radar and aircraft observations from CLARE'98, Q. J. R. Meteorol. Soc., 129, 2089–2116, https://doi.org/10.1256/rj.01.208, 2003.

Kiemle, C., Wirth, M., Fix, A., Rahm, S., Corsmeier, U., and Di Girolamo, P.: Latent heat flux measurements over complex terrain by airborne water vapour and wind lidars, Q. J. R. Meteorol. Soc., 137, 190–203, https://doi.org/10.1002/qj.757, 2011.

Konow, H., Ewald, F., George, G., Jacob, M., Klingebiel, M., Kölling, T., Luebke, A. E., Mieslinger, T., Pörtge, V., Radtke, J., Schäfer, M., Schulz, H., Vogel, R., Wirth, M., Bony, S., Crewell, S., Ehrlich, A., Forster, L., Giez, A., Gödde, F., Groß, S., Gutleben, M., Hagen, M., Hirsch, L., Jansen, F., Lang, T., Mayer, B., Mech, M., Prange, M., Schnitt, S., Vial, J., Walbröl, A., Wendisch, M., Wolf, K., Zinner, T., Zöger, M., Ament, F., and Stevens, B.: EUREC4A's HALO, Earth Syst. Sci. Data, 13, 5545–5563, https://doi.org/10.5194/essd-13-5545-2021, 2021.

Koren, I., Dror, T., Altaratz, O., and Chekroun, M. D.: Cloud Versus Void Chord Length Distributions (LvL) as a Measure for Cloud Field Organization, Geophys. Res. Lett., 51, e2024GL108435, https://doi.org/10.1029/2024GL108435, 2024.

Lee, K. O., Flamant, C., Ducrocq, V., Duffourg, F., Fourrié, N., Delanoë, J., and Bech, J.: Initiation and development of a mesoscale convective system in the Ebro River Valley and related heavy precipitation over northeastern Spain during HyMeX IOP 15a, Q. J. R. Meteorol. Soc., 143, 942–956, https://doi.org/10.1002/qj.2978, 2017.

LeMone, M. A. and Pennell, W. T.: The Relationship of Trade Wind Cumulus Distribution to Subcloud Layer Fluxes and Structure, Mon. Weather Rev., 104, 524–539, https://doi.org/https://doi.org/10.1175/1520-0493%281976%29104%3C0524%3ATROTWC%3E2.0.CO%3B2, 1976.

https://doi.org/10.5194/egusphere-2026-6720
Preprint. Discussion started: 5 November 2026
© Author(s) 2026. CC BY 4.0 License.



McGill, M., Hlavka, D., Hart, W., Scott, V. S., Spinhirne, J., and Schmid, B.: Cloud Physics Lidar: instrument description and initial measurement results, Appl. Opt., 41, 3725, https://doi.org/10.1364/ao.41.003725, 2002.

Nicolet, M.: On the molecular scattering in the terrestrial atmosphere : An empirical formula for its calculation in the homosphere, Planet. Space Sci., 32, 1467–1468, https://doi.org/10.1016/0032-0633(84)90089-8, 1984.

Pelon, J., Flamant, P., Mégie, G., and Meissonnier, W.: The LEANDRE project: a French airborne lidar system for meteorological studies, in: Proceedings of the 14th International Laser Radar Conference (ILRC), San Candido, Italy, 20–24 June 1988, Istituto di Ricerca sulle Onde Elettromagnetiche (IROE), Consiglio Nazionale delle Ricerche, Florence, Italy, 197–200, 1988.

Pelon, J., Flamant, C., Chazette, P., Leon, J.-F. J.-F., Tanre, D., Sicard, M., Satheesh, S. K., Tanré, D., Sicard, M., and Satheesh, S. K.: Characterization of aerosol spatial distribution and optical properties over the Indian Ocean from airborne LIDAR and radiometry during INDOEX'99, J. Geophys. Res., 107, 8029, https://doi.org/10.1029/2001JD000402, 2002.

Penney, C. M., St. Peters, R. L., and Lapp, M.: Absolute rotational Raman cross sections for N_2, O_2, and CO_2, J. Opt. Soc. Am., 64, 712, https://doi.org/10.1364/josa.64.000712, 1974.

Renger, W., Kiemle, C., Schreiber, H.-G., Wirth, M., and Moerl, P.: Correlative Measurements in Support of LITE Using the Airborne Backscatter LIDAR ALEX, in: Advances in Atmospheric Remote Sensing with Lidar, Springer, Berlin, Heidelberg, 165–168, https://doi.org/10.1007/978-3-642-60612-0_41, 1997.

Rogers, R. R., Hair, J. W., Hostetler, C. A., Ferrare, R. A., Obland, M. D., Cook, A. L., Harper, D. B., Burton, S. P., Shinozuka, Y., McNaughton, C. S., Clarke, A. D., Redemann, J., Russell, P. B., Livingston, J. M., and Kleinman, L. I.: NASA LaRC airborne high spectral resolution lidar aerosol measurements during MILAGRO: Observations and validation, Atmos. Chem. Phys., 9, 4811–4826, https://doi.org/10.5194/acp-9-4811-2009, 2009.

Royer, P., Chazette, P., Lardier, M., and Sauvage, L.: Aerosol content survey by mini N2-Raman lidar: Application to local and long-range transport aerosols, Atmos. Environ., 45, 7487–7495, https://doi.org/10.1016/j.atmosenv.2010.11.001, 2011.

Sherlock, V., Hauchecorne, A., and Lenoble, J.: Methodology for the independent calibration of Raman backscatter water-vapor lidar systems., Appl. Opt., 38, 5816–37, https://doi.org/10.1364/AO.38.005838, 1999.

Totems, J., Chazette, P., and Baron, A.: Mitigation of bias sources for atmospheric temperature and humidity in the mobile Raman Weather and Aerosol Lidar (WALI), Atmos. Meas. Tech., 14, 7525–7544, https://doi.org/10.5194/amt-14-7525-2021, 2021.

Whiteman, D. N.: Examination of the traditional Raman lidar technique I Evaluating the temperature-dependent lidar equations, Appl. Opt., 42, 2571, https://doi.org/10.1364/AO.42.002571, 2003.

Whiteman, D. N., Cadirola, M., Venable, D., Calhoun, M., Miloshevich, L., Vermeesch, K., Twigg, L., Dirisu, A., Hurst, D., Hall, E., Jordan, A., and Vömel, H.: Correction technique for Raman water vapor lidar signal-dependent bias and suitability for water vapor trend monitoring in the upper troposphere, Atmos. Meas. Tech., 5, 2893–2916, https://doi.org/10.5194/amt-5-2893-2012, 2012.

Wirth, M., Fix, A., Mahnke, P., Schwarzer, H., Schrandt, F., and Ehret, G.: The airborne multi-wavelength water vapor differential absorption lidar WALES: System design and performance, Appl. Phys. B Lasers Opt., 96, 201–213, https://doi.org/10.1007/s00340-009-3365-7, 2009.

Wu, D., Wang, Z., Wechsler, P., Mahon, N., Deng, M., Glover, B., Burkhart, M., Kuestner, W., and Heesen, B.: Airborne compact rotational Raman lidar for temperature measurement, Opt.

https://doi.org/10.5194/egusphere-2026-6720
Preprint. Discussion started: 5 November 2026
© Author(s) 2026. CC BY 4.0 License.



Express, 24, A1210, https://doi.org/10.1364/oe.24.0a1210, 2016.